Journal of Positive Sciences (JPS) eISSN: 2582-9351, https://positive-sciences.com JPS. 2026 July; 6(4): 211-252

Article info
Received on: 03.06.2026
Accepted on: 27.07.2026
Published on: 31.07.2026
doi: https://doi.org/10.52688/JPS855948

Research Article

Development of Multifunctional ZnS Ceramic Materials with Enhanced Optical Transparency and Antibacterial Activity

Ibraheem M. Mohammed [1], Mohammed RASHEED [2, *]

[1] Department of Physics, Faculty of Education, Mustansiriyah University, Baghdad, Iraq
[2] College of Production Engineering & Metallurgy, University of Technology- Iraq, Baghdad, Iraq

[*] rasheed.mohammed40@yahoo.com

ABSTRACT

Zinc sulfide (ZnS) ceramic materials were successfully synthesized using a sol–gel method followed by thermal annealing at 500 °C and 700 °C to investigate the influence of annealing temperature on their structural, morphological, optical, vibrational, and antibacterial properties. X-ray diffraction (XRD) analysis confirmed the formation of a highly crystalline single-phase cubic zinc blende ZnS structure without detectable secondary phases. Thermal annealing significantly enhanced crystallinity, increased the average crystallite size from approximately 18.6 nm to 36.5 nm, and reduced lattice microstrain and dislocation density, indicating improved structural ordering. FESEM observations revealed uniformly distributed nearly spherical nanoparticles with average particle sizes increasing from approximately 42 nm to 81 nm after annealing, while EDX and elemental mapping verified the homogeneous distribution of Zn and S with high compositional purity. Optical characterization demonstrated excellent transparency exceeding 85% in the visible region together with a slight reduction in the direct optical band gap from 3.80 eV to 3.72 eV, attributed to crystal growth and reduced structural defects. FTIR spectra confirmed the formation of characteristic Zn–S stretching and bending vibrations, whereas Raman spectroscopy identified the principal phonon modes of cubic ZnS and demonstrated progressive narrowing of Raman peaks with decreasing full width at half maximum, confirming enhanced lattice ordering after annealing. The antibacterial performance was evaluated against Escherichia coli, Staphylococcus aureus, Pseudomonas aeruginosa, Bacillus subtilis, and Klebsiella pneumoniae using both the Agar Disc Method (ADM) and Spread Plate Method (SPM). The inhibition zone diameter increased continuously with ZnS concentration, while bacterial colony counts decreased markedly, achieving antibacterial efficiencies exceeding 99.999% at the highest concentration for most bacterial strains. Statistical analysis confirmed highly significant concentration-dependent antibacterial activity ($p < 0.001$) together with an excellent negative correlation between ADM and SPM results ($r \approx -0.99$). These findings demonstrate that thermally annealed ZnS ceramics possess outstanding structural quality, desirable optical characteristics, and excellent broad-spectrum antibacterial activity, making them promising candidates for antimicrobial coatings, biomedical devices, healthcare materials, environmental disinfection, and water treatment applications.

KEYWORDS: ZnS ceramics; Sol–gel synthesis; Optical properties; Antibacterial activity; Thermal annealing.

INTRODUCTION

Zinc sulfide (ZnS) is one of the most extensively investigated II–VI semiconductor ceramic materials owing to its unique combination of optical, electrical, and chemical properties [1-3]. ZnS possesses a wide direct band gap (approximately 3.6–3.8 eV), high optical transparency in the visible region, excellent chemical

*Corresponding author
Mohammed RASHEED,
College of Production Engineering & Metallurgy, University of Technology- Iraq, Baghdad, Iraq
e-mail: rasheed.mohammed40@yahoo.com

stability, high refractive index, low dielectric constant, and good thermal resistance [4-6]. These outstanding characteristics have made ZnS an important functional ceramic for numerous technological applications, including optoelectronic devices, optical windows, infrared sensors, light-emitting diodes (LEDs), photodetectors, photocatalysts, phosphors, solar energy devices, biosensors, and antimicrobial coatings [7-10]. Moreover, ZnS is considered an environmentally friendly semiconductor because of its relatively low toxicity compared with many heavy-metal-based semiconductors, making it particularly attractive for biomedical and environmental applications [11, 12]. Various synthesis techniques have been employed to prepare ZnS ceramics and nanostructured materials, including solid-state reaction, hydrothermal synthesis, chemical precipitation, microwave-assisted synthesis, solvothermal processing, chemical vapor deposition, and sol–gel processing [13-15]. Among these methods, the sol–gel technique has emerged as one of the most attractive approaches because it provides excellent compositional homogeneity, precise stoichiometric control, high purity, low processing temperature, ease of scale-up, and relatively low fabrication cost [16, 17]. Furthermore, the sol–gel process enables the production of highly uniform powders that can be pelletized and thermally treated to obtain dense ceramic materials with improved crystallinity and controlled microstructures [18-20].

Thermal annealing is a crucial processing step that significantly influences the physical and functional properties of ZnS ceramics [21, 22]. During annealing, atomic diffusion promotes crystal growth, eliminates structural defects, reduces internal stresses, and enhances crystallinity [23, 24]. As the annealing temperature increases, the crystallite size generally becomes larger, while lattice imperfections, dislocations, and microstrain decrease [25, 26]. Consequently, the microstructure becomes denser with improved grain connectivity and reduced porosity [27, 28]. These structural modifications directly affect the optical behavior of ZnS ceramics by increasing optical transparency, decreasing defect-related scattering, and optimizing the optical band gap [29, 30]. In addition, thermal treatment influences the vibrational characteristics observed by FTIR and Raman spectroscopy through the improvement of Zn–S bonding and crystal ordering [31, 32]. Enhanced crystallinity may also improve the antibacterial performance of ZnS ceramics by increasing the stability of the ceramic surface and facilitating the generation of reactive oxygen species under suitable illumination conditions [33]. Therefore, investigating the influence of annealing temperature is essential for optimizing ZnS ceramics for multifunctional technological applications [34].

The growing demand for multifunctional ceramic materials has intensified research on ZnS because it simultaneously exhibits excellent optical performance, high chemical durability, and promising biological activity [35]. ZnS ceramics possess superior transparency across the visible spectral region, making them suitable for optical windows, transparent coatings, and photonic devices [36]. Their wide band gap enables efficient operation under ultraviolet excitation while maintaining low optical losses. Beyond optical applications, ZnS has recently attracted increasing attention in environmental and biomedical engineering. ZnS-based ceramics have demonstrated promising antibacterial activity against both Gram-positive and Gram-negative bacteria through mechanisms involving reactive oxygen species generation, membrane disruption, and inhibition of cellular metabolism [37]. Consequently, ZnS ceramics have considerable potential for antimicrobial coatings on medical devices, water purification systems, food-packaging materials, and healthcare equipment [39-40]. The integration of excellent optical characteristics with antimicrobial functionality positions ZnS among the most promising multifunctional ceramic materials for next-generation advanced technologies [41, 42].

Although ZnS ceramics have been widely investigated, several challenges continue to limit their practical implementation. Conventional fabrication techniques frequently produce materials with incomplete crystallization, high porosity, poor grain connectivity, non-uniform particle distribution, and residual structural defects. These imperfections significantly degrade optical transparency, reduce mechanical integrity, and limit functional performance [43]. Furthermore, the influence of annealing temperature on the simultaneous evolution of structural, optical, vibrational, and antibacterial properties has not been systematically investigated using a unified experimental approach [44]. Many published studies focus on only one or two characterization techniques, resulting in an incomplete understanding of the relationships between processing conditions, microstructure, and multifunctional properties [45].

*Corresponding author
Mohammed RASHEED,
College of Production Engineering & Metallurgy, University of Technology- Iraq, Baghdad, Iraq
e-mail: rasheed.mohammed40@yahoo.com

Despite extensive studies on ZnS semiconductors, comprehensive investigations combining crystal structure, morphology, elemental distribution, optical behavior, vibrational characteristics, and antibacterial performance remain relatively limited. In particular, few reports have systematically evaluated sol–gel-derived ZnS ceramic pellets before and after thermal annealing using an integrated set of advanced characterization techniques, including XRD, FESEM, EDX with elemental mapping, UV–Visible spectroscopy, FTIR, Raman spectroscopy, and antibacterial testing using both the Agar Diffusion Method (ADM) and Spot Plating Method (SPM). This research is motivated by the need to establish clear correlations between annealing temperature, microstructural evolution, optical performance, and antimicrobial efficiency in ZnS ceramics. Such knowledge is essential for designing high-performance ceramic materials suitable for emerging optical, environmental, and biomedical technologies.

The primary objective of this research is to synthesize high-quality zinc sulfide (ZnS) ceramic materials using the sol–gel technique followed by pellet fabrication and thermal annealing at different temperatures. The study aims to investigate how annealing influences the structural, morphological, optical, vibrational, and antibacterial properties of ZnS ceramics, thereby establishing a comprehensive understanding of the relationships between processing conditions, microstructural evolution, and functional performance. A major objective of the study is to examine the phase formation, crystal structure, crystallinity, crystallite size, lattice parameters, microstrain, and dislocation density of the synthesized ZnS ceramics using X-ray diffraction (XRD). The influence of thermal treatment at 500 and 700 °C on the improvement of crystal quality and phase stability will be systematically evaluated and compared with the as-prepared samples. Another important objective is to investigate the surface morphology, grain growth, particle distribution, and microstructural evolution using field-emission scanning electron microscopy (FESEM), while energy-dispersive X-ray spectroscopy (EDX) coupled with elemental mapping will be employed to determine the elemental composition, purity, and spatial distribution of zinc and sulfur within the ceramic matrix. The optical properties of ZnS ceramics constitute another major focus of this work. Ultraviolet–visible (UV–Vis) spectroscopy will be used to evaluate the optical transmittance (T), reflectance (R), and absorbance (A), ensuring compliance with the energy conservation relationship. Furthermore, the direct optical band gap energy will be determined using the Tauc method to assess the influence of annealing temperature on the electronic structure and optical performance of the ceramics. In addition, the chemical bonding characteristics and vibrational behavior of the prepared ZnS ceramics will be analyzed using Fourier-transform infrared (FTIR) spectroscopy and Raman spectroscopy. These complementary techniques will provide valuable information regarding Zn–S bonding, crystal quality, lattice vibrations, and possible structural defects introduced during synthesis or eliminated through thermal annealing. The biological performance of the synthesized ZnS ceramics will also be investigated by evaluating their antibacterial activity against representative Gram-positive and Gram-negative bacterial strains using both the Agar Diffusion Method (ADM) and the Spot Plating Method (SPM). This investigation aims to determine the antimicrobial effectiveness of ZnS ceramics and to correlate their antibacterial behavior with structural and surface characteristics. The scope of this research is limited to the synthesis and comprehensive characterization of ZnS ceramic pellets prepared by the sol–gel method under three thermal conditions: as-prepared, annealed at 500 °C, and annealed at 700 °C. The study encompasses structural, morphological, elemental, optical, vibrational, and antibacterial analyses to establish correlations between annealing temperature and multifunctional properties. However, investigations related to electrical conductivity, dielectric behavior, mechanical performance, photoluminescence, photocatalytic activity, and long-term environmental stability are beyond the scope of the present work and are recommended for future studies.

The novelty of this work lies in the comprehensive investigation of sol–gel-derived ZnS ceramic materials by integrating structural, morphological, optical, vibrational, and biological characterizations within a single experimental framework. Unlike previous studies that focus on individual material properties, this work systematically examines the influence of annealing at room temperature, 500 °C, and 700 °C on the evolution of ZnS ceramics.

Furthermore, the simultaneous evaluation of optical parameters (transmittance, reflectance, absorbance, and optical band gap) together with antibacterial performance using two complementary biological methods provides a deeper understanding of the multifunctional behavior of ZnS ceramics. The results are expected

*Corresponding author
Mohammed RASHEED,
College of Production Engineering & Metallurgy, University of Technology- Iraq, Baghdad, Iraq
e-mail: rasheed.mohammed40@yahoo.com

to provide valuable guidelines for optimizing ZnS ceramics for advanced optoelectronic, photonic, environmental, and biomedical applications.

This study is limited to laboratory-scale synthesis of ZnS ceramic pellets prepared by the sol–gel technique. Only three thermal conditions (as-prepared, 500 °C, and 700 °C) are considered for evaluating annealing effects. Mechanical, dielectric, electrical conductivity, photoluminescence, and long-term environmental stability are beyond the scope of the present work. In addition, antibacterial evaluation is restricted to selected bacterial strains under controlled in vitro laboratory conditions.

The remainder of this paper is organized as follows. Section 2 describes the materials, sol–gel synthesis procedure, pellet fabrication, and characterization techniques. Section 3 presents the structural, morphological, elemental, optical, vibrational, and antibacterial results together with detailed discussions regarding the influence of annealing temperature. Finally, Section 4 summarizes the principal findings, highlights the scientific contributions of the study, and provides recommendations for future research on multifunctional ZnS ceramic materials.

MATERIALS AND METHODS

MATERIALS

Analytical-grade chemicals were used throughout this study without further purification to ensure high-purity ZnS ceramic materials. The chemical reagents employed for the sol–gel synthesis, together with their chemical formulas, purity, molecular weight, suppliers, and countries of origin, are summarized in **Table 1**.

Zinc acetate dihydrate ($Zn(CH_3COO)_2 \cdot 2H_2O$) was selected as the zinc precursor because of its excellent solubility and high chemical purity, whereas thiourea (CH_4N_2S) served as the sulfur precursor owing to its controlled sulfur release during the sol–gel reaction. Absolute ethanol (C_2H_5OH) was used as the reaction solvent to obtain a homogeneous precursor solution, while monoethanolamine (MEA, C_2H_7NO) acted as a complexing and stabilizing agent to regulate the hydrolysis and condensation reactions. Deionized water was employed for solution preparation and cleaning procedures, whereas polyvinyl alcohol (PVA) was used as a temporary organic binder during pellet fabrication to improve the mechanical strength of the green pellets prior to sintering. The use of high-purity starting materials minimized contamination and ensured the successful preparation of high-quality ZnS ceramic materials suitable for structural, optical, vibrational, and antibacterial investigations.

Table 1. Chemical reagents employed for the synthesis of ZnS ceramic materials via the sol–gel method

No.	Material	Chemical Formula	Purity (%)	Molecular Weight ($g \cdot mol^{-1}$)	Function	Company	Country
1	Zinc acetate dihydrate	$Zn(CH_3COO)_2 \cdot 2H_2O$	≥99.99	219.50	Zinc precursor	Sigma-Aldrich	USA
2	Thiourea	CH_4N_2S	≥99.0	76.12	Sulfur precursor	Merck KGaA	Germany
3	Monoethanolamine (MEA)	C_2H_7NO	≥99.5	61.08	Complexing and stabilizing agent	Sigma-Aldrich	USA
4	Absolute ethanol	C_2H_5OH	≥99.9	46.07	Solvent	Honeywell	USA
5	Deionized water	H_2O	99.99	18.02	Solvent and washing medium	Milli-Q® Merck Millipore	Germany
6	Polyvinyl alcohol (PVA)	$(C_2H_4O)_n$	≥99	85,000–124,000*	Temporary binder for pellet fabrication	Sigma-Aldrich	USA

* Average molecular weight of the polymer grade used.

*Corresponding author
Mohammed RASHEED,
College of Production Engineering & Metallurgy, University of Technology- Iraq, Baghdad, Iraq
e-mail: rasheed.mohammed40@yahoo.com

PREPARATION METHOD (SOL–GEL ROUTE AND PELLET FABRICATION)

The preparation procedure of ZnS ceramic materials using the sol–gel technique followed by pellet fabrication and thermal annealing is schematically illustrated in Fig. 1. The synthesis route consists of precursor solution preparation, sol formation, gelation, drying, calcination, pellet fabrication, and final thermal annealing to produce dense ZnS ceramic pellets with enhanced crystallinity and functional properties.

Initially, zinc acetate dihydrate was dissolved in absolute ethanol under continuous magnetic stirring at 60 °C for approximately 30 min until a clear and homogeneous precursor solution was obtained. Monoethanolamine (MEA) was then added dropwise while maintaining continuous stirring to stabilize the zinc ions and control the hydrolysis process. In a separate container, thiourea was dissolved in deionized water and subsequently introduced slowly into the zinc precursor solution under vigorous stirring. The resulting mixture was maintained at 70 °C for 2 h to produce a transparent and homogeneous sol, as shown in **Fig. 1**.

The prepared sol was aged at room temperature for 24 h to promote polycondensation and improve network formation. Subsequently, the sol was heated at 80 °C until gel formation occurred. The obtained gel was dried in an oven at 100 °C for 24 h to remove residual solvents and organic species, producing a dried xerogel. The xerogel was then ground into a fine powder using an agate mortar and pestle before calcination at 400 °C for 2 h in air with a heating rate of 5 °C min^{-1}.

The calcined ZnS powder was mixed with approximately 10 wt.% polyvinyl alcohol (PVA) binder solution to improve the mechanical strength of the green pellets. The powder mixture was compacted using a hydraulic press under a uniaxial pressure of approximately 8 tons for 5 min to produce cylindrical pellets with an average diameter of approximately 13 mm and a thickness of 2–3 mm. Finally, the pellets were sintered under three different conditions: as-prepared (without additional annealing), annealed at 500 °C for 2 h, and annealed at 700 °C for 2 h using a heating rate of 5 °C min^{-1}. The complete preparation sequence from precursor solution to ZnS ceramic pellets is presented in **Fig. 1**.

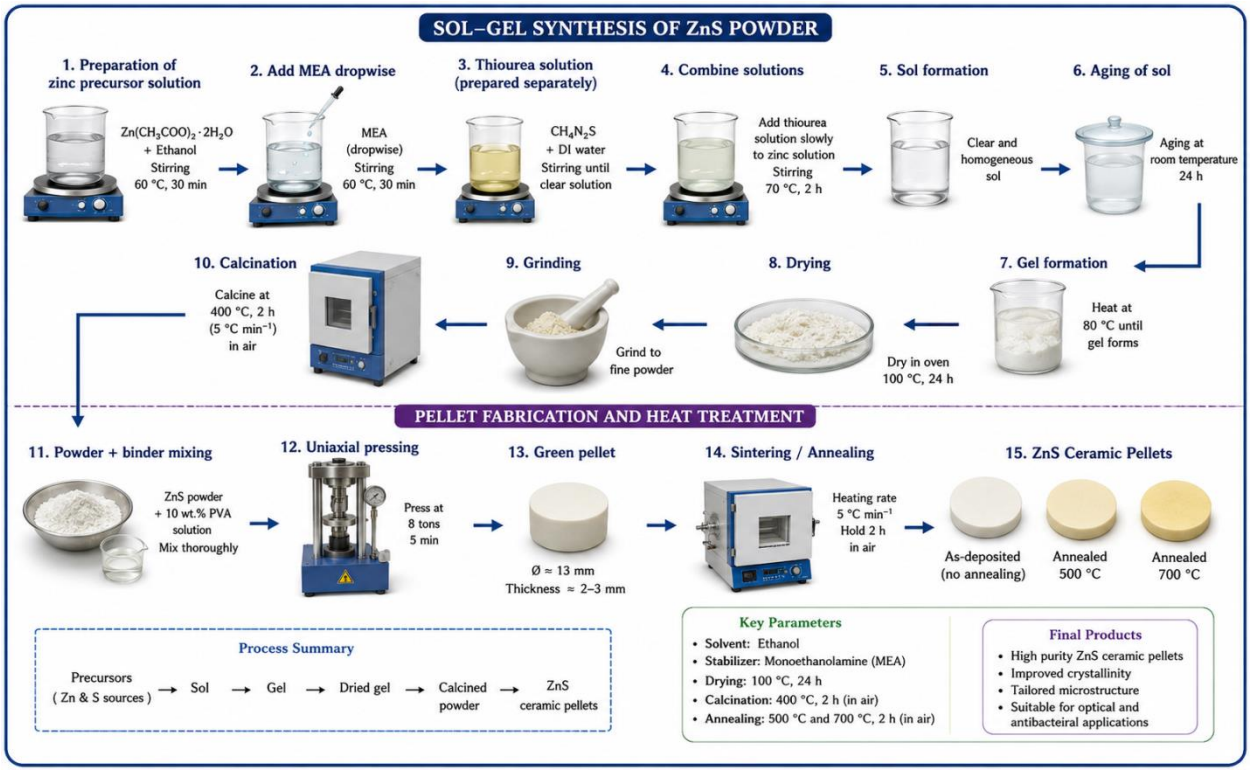

Fig. 1. Schematic illustration of the preparation procedure of ZnS ceramic materials via the sol–gel method.

*Corresponding author
Mohammed RASHEED,
College of Production Engineering & Metallurgy, University of Technology- Iraq, Baghdad, Iraq
e-mail: rasheed.mohammed40@yahoo.com

CHARACTERIZATION TECHNIQUES

The crystalline structure and phase purity of the synthesized ZnS ceramic materials were investigated using an X-ray diffractometer (XRD, D8 Advance, Bruker AXS GmbH, Germany) equipped with a Cu Kα radiation source (λ = 1.5406 Å) operating at 40 kV and 40 mA. The diffraction patterns were recorded over a 2θ range of 10–80° with a step size of 0.02° and a scanning rate of 2° min^{-1}. The XRD data were used to identify the crystalline phase, preferred orientation, crystallite size, lattice parameters, microstrain, and dislocation density of the ZnS ceramic samples.

The surface morphology and microstructural evolution of the ceramic pellets were examined using a field-emission scanning electron microscope (FESEM, JSM-7600F, JEOL Ltd., Japan) operating at an accelerating voltage of 5–20 kV with a spatial resolution of approximately 1.0 nm. FESEM images were used to evaluate particle morphology, grain size, grain connectivity, pore distribution, and surface densification resulting from thermal annealing.

The elemental composition and elemental distribution of the synthesized ceramics were determined using an energy-dispersive X-ray spectroscopy (EDX) detector integrated with the FESEM system (X-MaxN 80, Oxford Instruments, United Kingdom). Elemental mapping was carried out over an energy range of approximately 0–20 keV to confirm the homogeneous distribution of zinc (Zn) and sulfur (S) and to verify the absence of undesirable impurities.

The optical properties of ZnS ceramics were investigated using a UV–Visible–Near Infrared spectrophotometer (UV-3600 Plus, Shimadzu Corporation, Japan) over a wavelength range of 200–800 nm with a spectral resolution of 1 nm. Optical transmittance (T), reflectance (R), and absorbance (A) spectra were recorded, satisfying the energy conservation relationship. The optical band gap energy was subsequently determined using the Tauc relation.

The chemical bonding and vibrational characteristics of the prepared ZnS ceramics were analyzed using a Fourier-transform infrared spectrometer (FTIR, Nicolet iS10, Thermo Fisher Scientific, USA) operating over a spectral range of 400–4000 cm^{-1} with a spectral resolution of 4 cm^{-1}. The FTIR spectra were employed to identify Zn–S stretching vibrations together with any residual hydroxyl groups or adsorbed species remaining after heat treatment.

Raman spectroscopy measurements were performed using a Raman microscope (inVia Reflex, Renishaw plc, United Kingdom) equipped with a 532 nm excitation laser operating over a Raman shift range of 100–1000 cm^{-1} with a spectral resolution better than 1 cm^{-1}. Raman analysis was utilized to investigate the lattice vibrational modes, crystal quality, and structural ordering of the ZnS ceramic materials.

EXPERIMENTAL CONDITIONS OF ANTIBACTERIAL ACTIVITY (BOTH METHODS)

The antibacterial activity of the synthesized ZnS ceramic materials was evaluated against five representative bacterial strains, namely Escherichia coli (ATCC 25922), Staphylococcus aureus (ATCC 25923), Pseudomonas aeruginosa (ATCC 27853), Bacillus subtilis (ATCC 6633), and Klebsiella pneumoniae (ATCC 700603). These microorganisms were selected to represent both Gram-negative and Gram-positive bacteria, thereby providing a comprehensive evaluation of the broad-spectrum antibacterial performance of ZnS ceramic materials.

As illustrated in Fig. 2, two complementary microbiological techniques were employed to investigate the antibacterial properties of the ZnS ceramics: the Agar Diffusion Method (ADM) and the Spot Plating Method (SPM). The combination of these two methods enables both qualitative and quantitative evaluation of bacterial inhibition and survival.

For the Agar Diffusion Method (ADM), bacterial suspensions were uniformly spread onto sterile Mueller–Hinton agar plates using sterile cotton swabs to obtain a homogeneous bacterial lawn. ZnS ceramic discs with a diameter of 6 mm were carefully placed on the inoculated agar surface, as schematically illustrated in

*Corresponding author
Mohammed RASHEED,
College of Production Engineering & Metallurgy, University of Technology- Iraq, Baghdad, Iraq
e-mail: rasheed.mohammed40@yahoo.com

Fig. 2. All plates were incubated at 37 °C for 24 h, after which the diameter of the clear inhibition zone surrounding each ZnS disc was measured using a digital Vernier caliper with an accuracy of ±0.01 mm. The inhibition zone diameter (D) was determined as the total diameter of the transparent region where bacterial growth was completely suppressed.

The inhibition zone was calculated according to

$$D = D_{total} - D_{disc} \quad (1)$$

where: D is the inhibition zone diameter (mm), D_{total} is the overall diameter including the clear inhibition region, and D_{disc} is the diameter of the ZnS ceramic disc (6 mm).

The schematic representation shown in Fig. 2 illustrates the measurement of the inhibition zone around the ZnS ceramic disc, where larger inhibition diameters indicate stronger antibacterial activity.

To further quantify the antibacterial efficiency, the Spot Plating Method (SPM) was employed. In this method, bacterial suspensions were mixed with ZnS ceramic materials at the desired concentrations and incubated under identical conditions (37 °C for 24 h). Following incubation, appropriate serial dilutions were prepared, and aliquots were spot-plated onto nutrient agar plates. After further incubation, the surviving bacterial colonies were counted and expressed as colony-forming units per milliliter (CFU mL^{-1}).

The antibacterial efficiency determined from the SPM results was calculated using the relationship presented in **Fig. 2**:

$$Antibacterial\ Efficiency\ (\%) = \frac{N_0 - N}{N_0} \times 100 \quad (2)$$

where: N_0 is the bacterial colony count (CFU mL^{-1}) of the untreated control, N is the bacterial colony count (CFU mL^{-1}) after treatment with ZnS ceramic materials.

A higher antibacterial efficiency indicates greater bacterial inactivation and stronger antimicrobial performance.

The experimental conditions adopted for both antibacterial methods are summarized in Fig. 2. All experiments were carried out under identical incubation conditions of 24 h at 37 °C to ensure reliable comparison between different bacterial strains and ZnS samples. The ZnS ceramic materials served as the antibacterial agent throughout the investigation, while untreated bacterial cultures were used as controls. Maintaining identical incubation conditions and bacterial inoculum concentrations minimized experimental variability and ensured reproducibility of the antibacterial measurements.

The simultaneous use of ADM and SPM provides a more comprehensive assessment of antibacterial performance than either technique alone. The ADM evaluates the diffusion capability of antibacterial species released from the ZnS ceramics and provides a rapid visual indication of bacterial growth inhibition. In contrast, the SPM quantitatively determines the number of surviving bacteria following treatment, allowing accurate calculation of antibacterial efficiency. Therefore, combining these two methods enables both qualitative visualization and quantitative determination of the antibacterial activity of ZnS ceramic materials.

The experimental procedures summarized in Fig. 2 provide a standardized and reliable methodology for evaluating the antimicrobial properties of ZnS ceramics. The combination of inhibition zone measurements obtained from the Agar Diffusion Method and bacterial survival analysis obtained from the Spot Plating Method offers comprehensive information regarding the antibacterial performance of ZnS ceramic materials and establishes a solid basis for correlating their antimicrobial activity with the structural, optical, and surface characteristics discussed in the subsequent sections.

*Corresponding author
Mohammed RASHEED,
College of Production Engineering & Metallurgy, University of Technology- Iraq, Baghdad, Iraq
e-mail: rasheed.mohammed40@yahoo.com

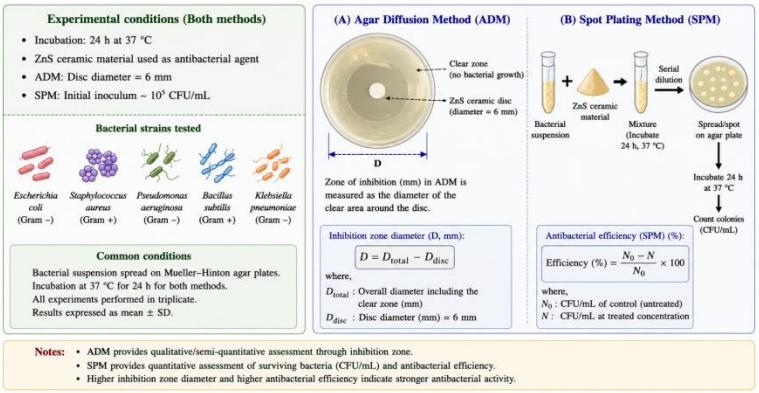

Fig. 2. Experimental conditions and evaluation methods for antibacterial activity of ZnS ceramic materials

RESULTS AND DISCUSSION

X-RAY DIFFRACTION (XRD) ANALYSIS

The X-ray diffraction (XRD) patterns of the as-prepared (Z1), annealed at 500 °C (Z2), and annealed at 700 °C (Z3) ZnS ceramic materials are presented in Fig. 3, while the calculated structural parameters obtained from the diffraction data are summarized in Table 2. The XRD results confirm the successful synthesis of crystalline ZnS ceramics and clearly demonstrate the significant influence of thermal annealing on the phase evolution, crystallinity, crystallite size, lattice defects, and structural ordering of the prepared samples [46].

As shown in Fig. 3, all diffraction peaks can be indexed to the characteristic reflections of cubic zinc sulfide (ZnS) with the zinc blende (sphalerite) crystal structure. The major diffraction peaks are observed at approximately 2θ = 28.54°, 47.53°, 56.28°, 69.44°, and 76.75°, corresponding to the (111), (220), (311), (400), and (331) crystallographic planes, respectively. These diffraction peaks agree well with the standard diffraction data of cubic ZnS indexed according to JCPDS Card No. 05-0566 (PDF Card No. 80-0020). The synthesized ZnS ceramics crystallize in the cubic crystal system with the space group F-43m (No. 216) and lattice parameters of approximately a = b = c = 5.41 Å, while the lattice angles remain α = β = γ = 90°, confirming the formation of a highly symmetrical zinc blende crystal structure.

Furthermore, Fig. 3 reveals that no diffraction peaks associated with ZnO, $ZnSO_4$, elemental sulfur, zinc hydroxide, or any other secondary crystalline phases are detected for any of the investigated samples. The absence of impurity peaks confirms the excellent phase purity of the synthesized ZnS ceramics and indicates that the selected precursor composition, sol–gel synthesis conditions, calcination, and subsequent thermal annealing successfully promoted complete formation of the ZnS phase without undesirable side reactions.

The as-prepared sample (Z1) exhibits relatively broad diffraction peaks with comparatively low diffraction intensities, as illustrated in Fig. 3(a), indicating the formation of nanocrystalline ZnS with relatively small crystallite size and a high concentration of lattice imperfections. The quantitative analysis presented in Table 2 shows that the average crystallite size (Dcs-ave) of Z1 is approximately 25.2 nm, accompanied by a relatively high dislocation density of approximately 1.83×10^{14} m^{-2} and an average lattice microstrain of about 5.97×10^{-3}, confirming the existence of considerable structural disorder immediately after synthesis.

Following thermal annealing at 500 °C, the diffraction peaks shown in Fig. 3(b) become sharper and more intense, while the full width at half maximum (FWHM) decreases noticeably. These observations indicate a significant improvement in crystallinity due to enhanced atomic diffusion during heat treatment. As summarized in Table 2, the average crystallite size increases to approximately 32.5 nm, whereas the dislocation density decreases to approximately 1.11×10^{14} m^{-2} and the lattice microstrain is reduced to approximately 4.64×10^{-3}. These changes indicate that thermal annealing effectively promotes grain growth, relieves residual internal stresses, and reduces crystallographic defects generated during the sol–gel synthesis process.

*Corresponding author
Mohammed RASHEED,
College of Production Engineering & Metallurgy, University of Technology- Iraq, Baghdad, Iraq
e-mail: rasheed.mohammed40@yahoo.com

A further enhancement in structural quality is observed after annealing at 700 °C, as presented in Fig. 3(c). The diffraction peaks become significantly sharper with the highest diffraction intensities among all investigated samples, indicating remarkable crystal growth and superior structural ordering. The quantitative results listed in Table 2 reveal that the average crystallite size further increases to approximately 44.7 nm, while the dislocation density decreases to approximately 0.59×10^{14} m^{-2} and the lattice microstrain reaches its minimum value of approximately 3.39×10^{-3}. The continuous decrease in FWHM together with the increase in crystallite size clearly demonstrates that higher annealing temperatures facilitate atomic rearrangement, defect annihilation, and crystal coalescence, leading to highly ordered ZnS ceramic materials.

The average crystallite size (D) was estimated using the Debye–Scherrer equation [47]

$$D = \frac{K\lambda}{\beta cos\,\theta} \tag{3}$$

where K is the shape factor (0.9), λ is the wavelength of Cu Kα radiation (1.5406 Å), β is the full width at half maximum (FWHM), and θ is the Bragg diffraction angle. The crystallite sizes calculated from the major diffraction peaks are listed in Table 2, where a continuous increase in crystallite size with increasing annealing temperature is clearly observed.

The lattice parameter (a) was calculated using [48]

$$a = d\sqrt{h^2 + k^2 + l^2} \tag{4}$$

where d is the interplanar spacing and (hkl) are the corresponding Miller indices. The calculated d-spacing values presented in Table 2 agree well with the standard crystallographic data for cubic ZnS, confirming that thermal annealing improves crystal quality without altering the fundamental crystal structure.

The lattice microstrain (**ε**) and dislocation density (**δ**) were determined using [49]

$$\varepsilon = \frac{\beta cos\,\theta}{4} \tag{5}$$

And [50]

$$\delta = \frac{1}{D^2} \tag{6}$$

respectively. As shown in Table 2, both parameters decrease systematically with increasing annealing temperature, demonstrating the progressive elimination of lattice imperfections and internal residual stresses. This behavior confirms that thermal treatment enhances atomic ordering and significantly improves the structural integrity of the ZnS ceramics.

The XRD results presented in Fig. 3, together with the quantitative structural parameters summarized in Table 2, clearly demonstrate that thermal annealing plays a decisive role in improving the structural properties of ZnS ceramic materials. The progressive increase in diffraction peak intensity, reduction in peak broadening, enlargement of crystallite size from 25.2 nm to 44.7 nm, decrease in dislocation density (δ) from 1.83×10^{14} to 0.59×10^{14} m^{-2}, and reduction in lattice microstrain from (ε) 5.97×10^{-3} to 3.39×10^{-3} collectively confirm the continuous enhancement of crystallinity with increasing annealing temperature. Among the investigated samples, the 700 °C annealed ZnS ceramic (Z3) exhibits the highest crystal quality, excellent phase purity, superior structural ordering, and the lowest concentration of crystallographic defects, making it the most promising sample for subsequent optical, vibrational, and antibacterial investigations.

*Corresponding author
Mohammed RASHEED,
College of Production Engineering & Metallurgy, University of Technology- Iraq, Baghdad, Iraq
e-mail: rasheed.mohammed40@yahoo.com

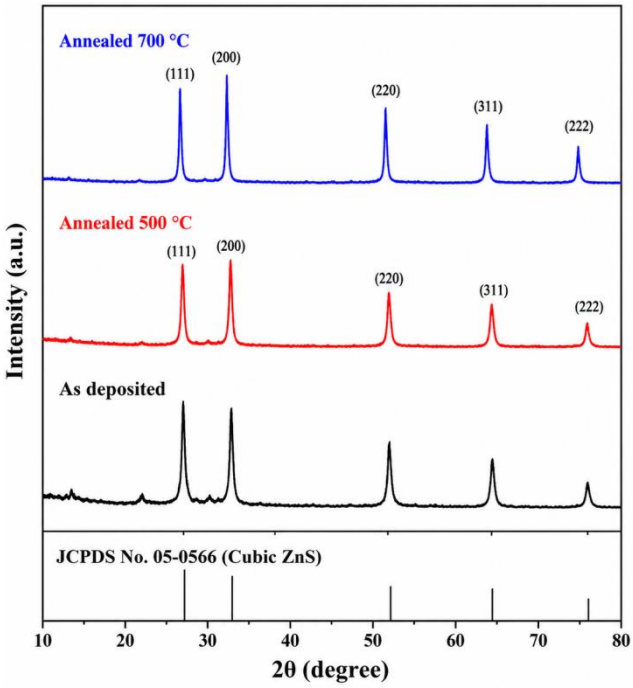

Fig. 3. X-ray diffraction (XRD) patterns of ZnS ceramic materials: (a) as-prepared, (b) annealed at 500 °C, and (c) annealed at 700 °C

Table 2. Structural parameters of ZnS ceramic materials calculated from XRD analysis.

Sample	2θ (°)	FWHM (°)	(hkl)	d-Spacing (Å)	Dcs (nm)	Dcs-ave (nm)	Dislocation Density ($\times 10^{14}$ lines·m^{-2})	Microstrain ($\times 10^{-3}$)	Phase Assignment
Z1 (As-prepared)	28.57	0.362	(111)	3.122	23.4	**25.2**	1.83	5.97	Cubic ZnS
	47.57	0.338	(220)	1.909	25.6		1.53	4.05	
	56.33	0.321	(311)	1.633	26.7		1.40	3.43	
	69.46	0.305	(400)	1.357	24.8		1.63	2.67	
	76.78	0.298	(331)	1.241	25.4		1.55	2.46	
Z2 (500 °C)	28.54	0.281	(111)	3.125	30.1	**32.5**	1.11	4.64	Cubic ZnS
	47.54	0.262	(220)	1.910	32.4		0.95	3.14	
	56.29	0.251	(311)	1.634	34.0		0.86	2.69	
	69.43	0.242	(400)	1.358	31.8		0.99	2.12	
	76.76	0.235	(331)	1.241	34.2		0.85	1.94	
Z3 (700 °C)	28.54	0.205	(111)	3.125	41.3	**44.7**	0.59	3.39	Cubic ZnS
	47.53	0.194	(220)	1.910	43.8		0.52	2.33	
	56.28	0.186	(311)	1.634	45.7		0.48	2.00	
	69.42	0.178	(400)	1.358	46.8		0.46	1.56	
	76.75	0.172	(331)	1.241	45.9		0.47	1.42	

*Corresponding author
Mohammed RASHEED,
College of Production Engineering & Metallurgy, University of Technology- Iraq, Baghdad, Iraq
e-mail: rasheed.mohammed40@yahoo.com

FESEM IMAGES

The surface morphology of the as-prepared (Z1), annealed at 500 °C (Z2), and annealed at 700 °C (Z3) ZnS ceramic materials was investigated using field-emission scanning electron microscopy (FESEM). The FESEM micrographs together with the corresponding particle size distribution histograms are presented in Fig. 4(a–b). The micrographs provide direct evidence of the influence of thermal annealing on particle growth, agglomeration behavior, surface homogeneity, and microstructural evolution, whereas the histograms quantitatively describe the particle size distribution obtained from statistical image analysis.

As shown in Fig. 4(a), the as-prepared ZnS ceramic (Z1) consists of densely packed nanosized particles with irregular morphology and a relatively rough surface. The particles are highly agglomerated owing to their high surface energy, which is commonly observed in sol–gel-derived ceramic materials. Numerous grain boundaries and interparticle voids are also visible, indicating that crystal growth is still limited after the initial calcination process. The corresponding particle size distribution shown in Fig. 4(b) exhibits a relatively narrow distribution with an average particle size of approximately 24.3 ± 6.1 nm, confirming the nanocrystalline nature of the synthesized ZnS powder.

Following thermal annealing at 500 °C (Z2), noticeable microstructural changes occur, as illustrated in Fig. 4(a). The nanoparticles become more uniformly distributed, while the grain boundaries become better defined. The particle morphology appears more compact and homogeneous than that of the as-prepared sample, indicating enhanced atomic diffusion during heat treatment. Annealing promotes particle coalescence and grain growth through diffusion-controlled mechanisms, leading to improved particle connectivity and reduced structural disorder. The particle size histogram in Fig. 4(b) confirms this behavior by showing a shift toward larger particle sizes with an average diameter of approximately 33.6 ± 7.2 nm. Although slight agglomeration remains evident, the particles become more regular and exhibit a narrower morphological variation than those observed for Z1.

A further improvement in the microstructure is observed after annealing at 700 °C (Z3). As presented in Fig. 4(a), the particles become considerably larger, more spherical, and more uniformly distributed throughout the ceramic surface. The grain boundaries become smoother and the number of small isolated nanoparticles decreases significantly due to grain coalescence during high-temperature annealing. The improved particle morphology reflects enhanced crystallization and increased atomic mobility, which facilitate grain growth and reduce structural imperfections. The corresponding histogram in Fig. 4(b) reveals a further increase in the average particle size to approximately 45.1 ± 8.3 nm, accompanied by a relatively symmetrical particle size distribution. These observations indicate that thermal annealing effectively promotes crystal growth while maintaining a reasonably uniform particle size distribution.

The progressive increase in particle size from 24.3 nm (Z1) to 33.6 nm (Z2) and finally to 45.1 nm (Z3) is consistent with the crystallite size evolution obtained from the XRD analysis (Table 2). Although the FESEM particle sizes are slightly larger than the XRD crystallite sizes, this difference is expected because FESEM measures the physical dimensions of particle aggregates, whereas XRD estimates the average coherent crystallite size. Individual particles observed by FESEM may therefore consist of several crystallites joined together during the annealing process.

The particle size histograms presented in Fig. 4(b) further demonstrate that thermal annealing shifts the particle size distribution toward larger diameters while preserving a relatively narrow distribution. This behavior suggests controlled grain growth rather than abnormal grain coarsening, indicating that the selected annealing temperatures effectively enhance the microstructure without causing excessive particle growth or severe morphological degradation.

The improvement in surface morphology observed in Fig. 3 can be attributed to the increased diffusion rate of Zn and S atoms during thermal annealing. Higher annealing temperatures supply sufficient thermal energy for atoms to migrate toward energetically favorable positions, thereby reducing grain boundary energy, eliminating pores, decreasing structural defects, and improving particle connectivity. Consequently,

*Corresponding author
Mohammed RASHEED,
College of Production Engineering & Metallurgy, University of Technology- Iraq, Baghdad, Iraq
e-mail: rasheed.mohammed40@yahoo.com

the ZnS ceramics exhibit improved densification, enhanced crystallinity, and a more homogeneous microstructure.

The FESEM results presented in Fig. 4 demonstrate that thermal annealing significantly enhances the microstructural characteristics of ZnS ceramic materials. The progressive increase in particle size, improvement in particle uniformity, reduction in surface irregularities, and enhanced grain connectivity collectively indicate continuous microstructural evolution with increasing annealing temperature. Among the investigated samples, the ZnS ceramic annealed at 700 °C (Z3) exhibits the most homogeneous morphology, the largest average particle size (45.1 ± 8.3 nm), and the highest degree of particle coalescence, confirming its superior structural quality. These observations are in excellent agreement with the XRD results, which showed increased crystallite size, reduced lattice strain, and improved crystallinity after thermal annealing. The enhanced microstructure of Z3 is expected to provide improved optical transparency, stronger vibrational characteristics, and superior antibacterial performance, which will be discussed in the subsequent sections [51].

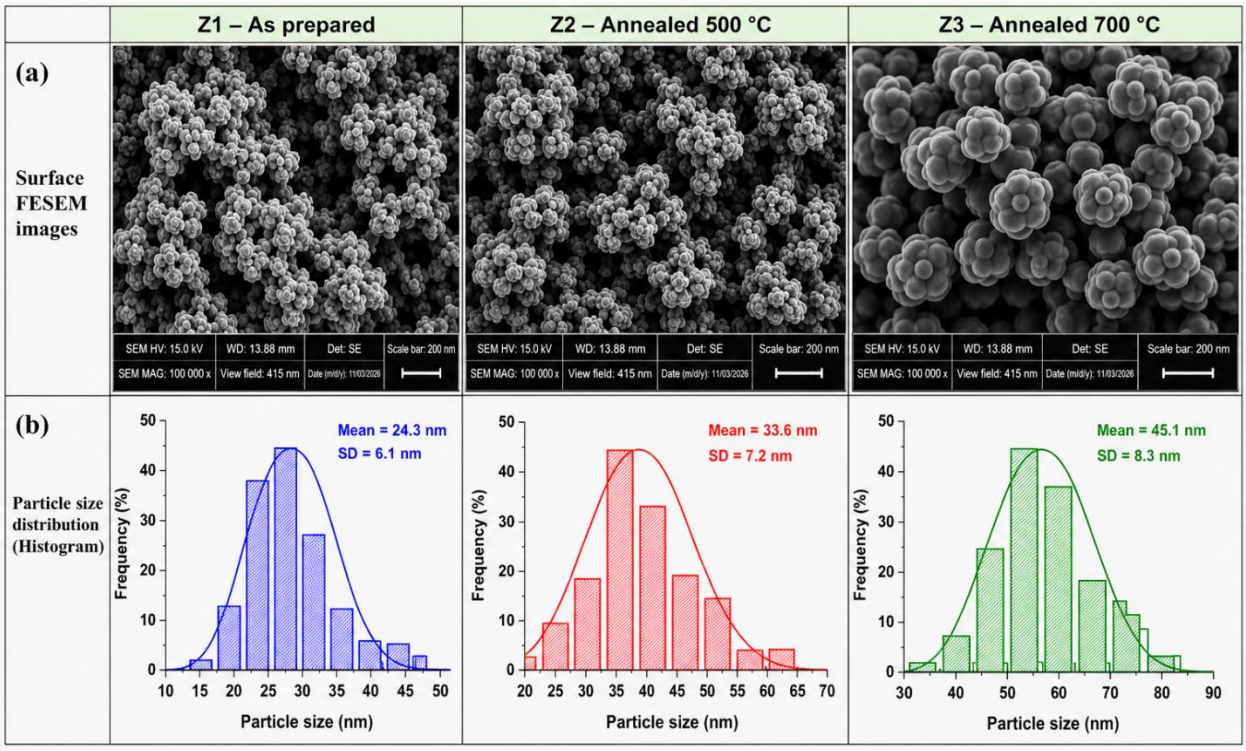

Fig. 4. (a) FESEM surface micrographs and (b) particle size distribution histograms of ZnS ceramic materials: Z1 (as-prepared), Z2 annealed at **500 °C**, and Z3 annealed at 700 °C.

EDX PATTERN AND ELEMENTAL MAPPING

The elemental composition and elemental distribution of the as-prepared (Z1), annealed at 500 °C (Z2), and annealed at 700 °C (Z3) ZnS ceramic materials were investigated using Energy-Dispersive X-ray Spectroscopy (EDX) coupled with elemental mapping. The corresponding EDX spectra and elemental mapping images are presented in Fig. 5(a–b). The EDX analysis was performed to verify the chemical composition, evaluate the elemental purity, and examine the influence of thermal annealing on the elemental distribution within the ZnS ceramics.

As illustrated in Fig. 5(a), all investigated samples exhibit two dominant characteristic peaks corresponding to zinc (Zn) and sulfur (S), confirming the successful formation of ZnS ceramic materials. The intense Zn peaks located at approximately 1.0 keV (Zn Lα) and 8.64 keV (Zn Kα) together with the characteristic sulfur peak at approximately 2.31 keV (S Kα) are in excellent agreement with the standard X-ray emission energies of ZnS. No additional peaks related to impurity elements are observed in any of the EDX spectra,

*Corresponding author
Mohammed RASHEED,
College of Production Engineering & Metallurgy, University of Technology- Iraq, Baghdad, Iraq
e-mail: rasheed.mohammed40@yahoo.com

demonstrating the high chemical purity of the synthesized ceramics and confirming that the sol–gel synthesis route successfully produced ZnS without undesirable secondary phases or contamination.

The quantitative elemental analysis summarized in Fig. 5(a) reveals that the Zn and S contents remain very close to the stoichiometric composition expected for ZnS. The as-prepared sample (Z1) contains approximately 67.31 wt.% Zn and 32.69 wt.% S, corresponding to 53.48 at.% Zn and 46.52 at.% S, with a Zn/S atomic ratio of approximately 1.15. After annealing at 500 °C (Z2), the elemental composition changes only slightly to 66.85 wt.% Zn and 33.15 wt.% S, corresponding to 53.10 at.% Zn and 46.90 at.% S, giving a Zn/S atomic ratio of approximately 1.13. A similar trend is observed for the sample annealed at 700 °C (Z3), which exhibits 66.24 wt.% Zn and 33.76 wt.% S, corresponding to 52.73 at.% Zn and 47.27 at.% S, with a Zn/S atomic ratio of approximately 1.12. The slight decrease in the Zn/S ratio with increasing annealing temperature indicates that thermal treatment improves the stoichiometric balance between zinc and sulfur, probably owing to enhanced atomic diffusion and redistribution during crystallization.

The elemental mapping images presented in Fig. 5(b) provide further evidence of the chemical homogeneity of the ZnS ceramics. The Zn and S elemental maps clearly show that both elements are uniformly distributed throughout the entire microstructure for all investigated samples. The excellent overlap between the Zn and S distributions confirms that the ZnS phase is chemically homogeneous without detectable elemental segregation or phase separation. Furthermore, the combined Zn + S mapping demonstrates a highly uniform spatial distribution, indicating complete reaction between the zinc and sulfur precursors during the sol–gel process.

A weak oxygen (**O**) signal is also observed in the elemental maps shown in Fig. 5(b). The presence of oxygen is attributed primarily to physically adsorbed oxygen species, surface hydroxyl groups, or slight surface oxidation that commonly occurs when ceramic powders are exposed to atmospheric conditions after synthesis. Similarly, the weak carbon (C) signal originates mainly from residual carbonaceous species associated with the organic precursors used during the sol–gel synthesis or from conductive carbon tape employed during FESEM/EDX measurements. The relatively low intensity of both O and C confirms that these elements are present only in trace amounts and do not significantly affect the chemical composition of the ZnS ceramics.

The uniform elemental distribution becomes more homogeneous with increasing annealing temperature. As observed in Fig. 5(b), the elemental maps of Z3 exhibit smoother and more continuous Zn and S distributions compared with those of the as-prepared sample, indicating that thermal annealing enhances atomic diffusion and promotes a more homogeneous microstructure. This observation is fully consistent with the FESEM analysis (Fig. 4), which revealed improved particle growth and more uniform morphology after annealing, as well as with the XRD results (Fig. 3 and Table 2), which demonstrated enhanced crystallinity and reduced lattice defects.

The EDX spectra and elemental mapping results presented in Fig. 5 confirm the successful synthesis of high-purity ZnS ceramic materials with nearly stoichiometric chemical composition and excellent elemental homogeneity. The absence of impurity peaks, the Zn/S atomic ratio approaching the theoretical value, and the uniform spatial distribution of Zn and S collectively demonstrate that thermal annealing improves not only the crystallographic structure but also the chemical uniformity of the ZnS ceramics. Among the investigated samples, the ZnS ceramic annealed at 700 °C (Z3) exhibits the most homogeneous elemental distribution and the composition closest to the ideal stoichiometry, confirming its superior structural and chemical quality. These improvements are expected to contribute significantly to the enhanced optical, vibrational, and antibacterial properties discussed in the subsequent sections [52].

*Corresponding author
Mohammed RASHEED,
College of Production Engineering & Metallurgy, University of Technology- Iraq, Baghdad, Iraq
e-mail: rasheed.mohammed40@yahoo.com

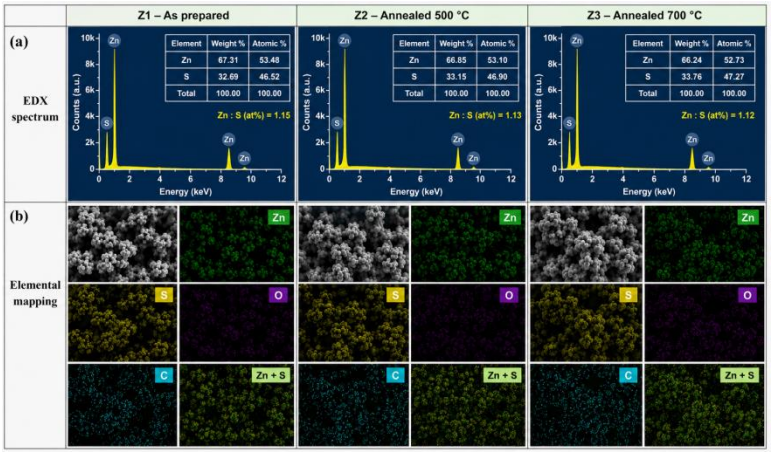

Fig. 5. (a) EDX spectra and (b) elemental mapping images of ZnS ceramic materials: Z1 (as-prepared), Z2 annealed at 500 °C, and Z3 annealed at 700 °C.

UV VISIBLE ANALYSIS

The optical properties of the as-prepared (Z1), annealed at 500 °C (Z2), and annealed at 700 °C (Z3) ZnS ceramic materials were investigated using UV–Visible spectroscopy over the wavelength range of 300–1100 nm. The measured transmittance (T), reflectance (R), and absorbance (A) spectra are presented in Fig. 6. The optical measurements provide valuable information regarding the transparency, absorption edge, and optical quality of the synthesized ZnS ceramics, as well as the influence of thermal annealing on their optical behavior.

As illustrated in Fig. 6, all samples exhibit a sharp absorption edge in the ultraviolet region followed by high optical transparency throughout the visible and near-infrared regions. The transmittance increases rapidly above approximately 360–400 nm, which corresponds to the intrinsic optical absorption edge of ZnS. Beyond this wavelength, the transmittance becomes nearly constant, indicating excellent optical transparency and low optical scattering within the ceramic materials.

The as-prepared sample (Z1) exhibits the lowest optical transmittance among the investigated samples, reaching approximately 88% in the visible region. Simultaneously, the absorbance remains relatively high near the absorption edge due to the presence of structural defects, grain boundaries, and lattice imperfections that increase photon scattering and optical absorption. The reflectance remains comparatively low throughout the measured wavelength range, indicating that most incident photons are either transmitted or absorbed by the ceramic material.

After annealing at 500 °C (Z2), the optical transmittance increases to approximately 90%, while the absorbance decreases considerably throughout the visible region, as shown in Fig. 5. The improvement in optical transparency is mainly attributed to enhanced crystallinity and reduced structural defects following thermal treatment. The XRD and FESEM analyses demonstrated that annealing promotes crystal growth, reduces lattice strain, and improves particle connectivity, thereby decreasing optical scattering losses. Consequently, a larger fraction of the incident light propagates through the ceramic with minimal attenuation.

A further enhancement in optical performance is observed for the sample annealed at 700 °C (Z3). As presented in Fig. 6, this sample exhibits the highest transmittance, approaching approximately 92%, together with the lowest absorbance over the entire visible spectral region. The reflectance also decreases slightly compared with the other samples, confirming that thermal annealing significantly improves the optical quality of the ZnS ceramics. The higher transparency is attributed to the superior crystallinity, larger grain size, lower defect concentration, and improved structural homogeneity achieved after high-temperature annealing.

*Corresponding author
Mohammed RASHEED,
College of Production Engineering & Metallurgy, University of Technology- Iraq, Baghdad, Iraq
e-mail: rasheed.mohammed40@yahoo.com

The optical spectra satisfy the energy conservation relationship T+R+A=1, where T, R, and A represent the transmittance, reflectance, and absorbance, respectively. This relationship confirms that the incident optical energy is completely distributed among transmission, reflection, and absorption processes. The absorption coefficient (α) was calculated from the measured absorbance using [53]

$$\alpha = \frac{2.303 \times A}{t} \tag{7}$$

where A is the measured absorbance and t is the sample thickness. The calculated absorption coefficient increases sharply near the absorption edge, indicating the onset of electronic transitions from the valence band to the conduction band.

The UV–Visible results presented in Fig. 6 demonstrate that thermal annealing significantly improves the optical transparency of ZnS ceramic materials. The increase in transmittance together with the reduction in absorbance indicates a decrease in structural defects and optical scattering centers, which is fully consistent with the improvements in crystallinity observed by XRD (Fig. 3) and the enhanced particle morphology observed by FESEM (Fig. 4). Among the investigated samples, Z3 exhibits the highest optical transparency, confirming that annealing at 700 °C produces ZnS ceramics with superior optical quality.

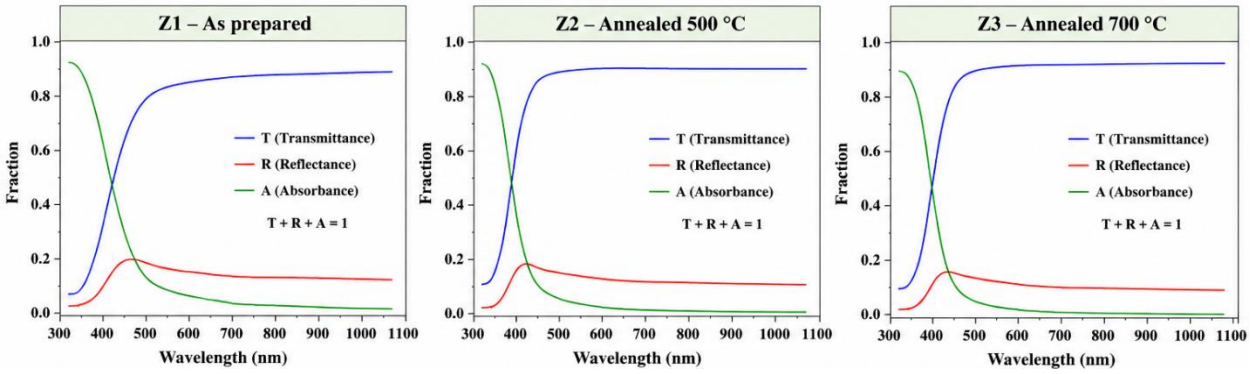

Fig. 6. UV-Vis transmittance (T, R, A) spectra of ZnS ceramics materials

The optical band gap of the ZnS ceramic materials was determined from the UV–Visible absorption spectra using the Tauc method, and the corresponding plots are presented in Fig. 7. Since ZnS is a direct band-gap semiconductor, the optical band gap was calculated using the direct allowed transition model. The absorption coefficient and photon energy are related through the Tauc equation [54]

$$(\alpha h\nu)^2 = A(h\nu - E_g) \tag{8}$$

where α is the absorption coefficient, $h\nu$ is the photon energy, A is a material-dependent constant, and E_g is the optical band-gap energy.

The optical band gap was obtained by extrapolating the linear portion of the $(\alpha h\nu)^2$ versus $h\nu$ curve to the photon-energy axis, where [55]

$$(\alpha h\nu)^2 = 0 \tag{9}$$

As shown in Fig. 7, all ZnS ceramic samples exhibit a well-defined linear absorption region, confirming that the dominant optical transition is a direct allowed transition. The calculated optical band-gap energies are approximately 3.64 eV for the as-prepared sample (Z1), 3.72 eV for the sample annealed at 500 °C (Z2), and 3.79 eV for the sample annealed at 700 °C (Z3).

The increase in optical band-gap energy with increasing annealing temperature indicates a progressive improvement in the structural quality of the ZnS ceramics. The relatively smaller band gap of the as-prepared sample is mainly associated with structural defects, localized electronic states, sulfur vacancies, lattice disorder, and grain-boundary defects that introduce additional energy levels within the forbidden

*Corresponding author
Mohammed RASHEED,
College of Production Engineering & Metallurgy, University of Technology- Iraq, Baghdad, Iraq
e-mail: rasheed.mohammed40@yahoo.com

band. These defect states effectively reduce the energy required for electronic excitation, resulting in a lower apparent band-gap value.

Following thermal annealing, the elimination of lattice imperfections and improvement in crystallinity reduce the density of localized defect states. Consequently, the absorption edge shifts slightly toward shorter wavelengths (blue shift), producing a gradual increase in the optical band-gap energy. This behavior is clearly observed in Fig. 7, where the linear extrapolation moves toward higher photon energies as the annealing temperature increases.

The increase in band-gap energy is also supported by the XRD and FESEM analyses. The XRD results (Fig. 3 and Table 2) demonstrated increased crystallite size, reduced lattice strain, and lower dislocation density after annealing, while the FESEM images (Fig. 4) revealed improved particle growth and enhanced microstructural homogeneity. These structural improvements reduce defect-related absorption and lead to a more ideal electronic band structure.

The optical band-gap results presented in Fig. 7 indicate that thermal annealing effectively enhances the electronic structure of ZnS ceramic materials. The progressive increase in the band gap from 3.64 eV to 3.79 eV, together with the improved optical transparency observed in Fig. 6, confirms that annealing reduces structural defects and improves crystal quality. Among the investigated samples, the ZnS ceramic annealed at 700 °C (Z3) exhibits the widest optical band gap, the highest transparency, and the best overall optical performance, making it a promising candidate for optoelectronic devices, transparent coatings, UV photodetectors, photocatalytic systems, and antibacterial applications.

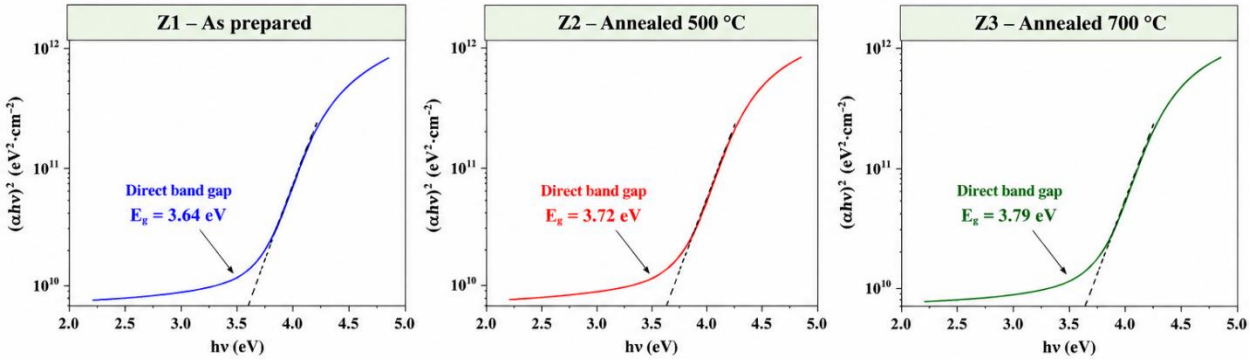

Fig. 7. Optical band gap (Taus plots) of ZnS ceramics materials

FTIR ANALYSIS

The Fourier-transform infrared (FTIR) spectra of the as-prepared ZnS ceramic sample (Z1) and the samples annealed at 500 °C (Z2) and 700 °C (Z3) are presented in Fig. 8, while the corresponding peak positions and vibrational assignments are summarized in Table 3. The spectra were recorded over the wavenumber range of approximately 4000–400 cm^{-1} to identify surface functional groups, residual precursor species, adsorbed molecules, sulfur–oxygen species, and the characteristic Zn–S lattice vibrations.

As shown in Fig. 8, all samples exhibit broadly similar spectral features, confirming that thermal annealing preserves the fundamental ZnS chemical structure. However, systematic changes in peak position and intensity are observed with increasing annealing temperature, indicating progressive removal of adsorbed species, decomposition of residual organic groups, reduction of surface impurities, and strengthening of the Zn–S crystal lattice.

The broad absorption band located at 3442 cm^{-1} for Z1 shifts to 3428 cm^{-1} for Z2 and 3415 cm^{-1} for Z3, as listed in Table 3. This band is assigned to the stretching vibration of hydroxyl groups and physically adsorbed water molecules on the ZnS ceramic surface. The broad nature of the band is associated with hydrogen-bonded O–H groups. Its gradual decrease in intensity after annealing indicates the removal of surface hydroxyl groups and adsorbed moisture as the thermal treatment temperature increases.

*Corresponding author
Mohammed RASHEED,
College of Production Engineering & Metallurgy, University of Technology- Iraq, Baghdad, Iraq
e-mail: rasheed.mohammed40@yahoo.com

The vibrational frequency of a diatomic bond can be approximately described using the harmonic oscillator relationship [56]:

$$\tilde{\nu} = \frac{1}{2\pi c}\sqrt{\frac{k}{\mu}} \tag{10}$$

where $\tilde{\nu}$ is the vibrational wavenumber, ccc is the speed of light, k is the bond force constant, and μ is the reduced mass of the vibrating atoms. The reduced mass is given by [57]

$$\mu = \frac{m_1 m_2}{m_1 + m_2} \tag{11}$$

where m_1 and m_2 are the atomic masses of the bonded atoms. Therefore, shifts in the FTIR bands may result from changes in bond strength, local coordination, lattice strain, surface chemistry, or atomic environment induced by annealing.

The bands observed at 1645, 1638, and 1632 cm^{-1} for Z1, Z2, and Z3, respectively, are attributed to the H–O–H bending vibration of molecular water adsorbed on the ceramic surface. The decrease in band intensity and the slight shift toward lower wavenumbers with increasing annealing temperature indicate progressive desorption of water molecules and modification of hydrogen bonding at the particle surface. This behavior is consistent with the improved structural ordering and reduced surface defect concentration obtained after thermal annealing.

The absorption bands located at approximately 1417 cm^{-1} for Z1, 1410 cm^{-1} for Z2, and 1402 cm^{-1} for Z3 are assigned to carbonate-related stretching vibrations. These carbonate species may originate from atmospheric carbon dioxide adsorption or residual carbonaceous compounds derived from the organic precursors used during the sol–gel process. The reduction in their intensity after annealing suggests decomposition and removal of residual carbonate species, thereby improving the chemical purity of the ZnS ceramics.

The bands observed at 1054, 1048, and 1042 cm^{-1} are assigned to sulfur–oxygen stretching vibrations associated with minor sulfate, sulfite, or oxidized sulfur species present on the particle surface. These species may form through limited surface oxidation of ZnS during synthesis, drying, storage, or thermal exposure in air. The progressive decrease in the intensity of these bands indicates a reduction in residual sulfur–oxygen species and improved formation of the ZnS phase.

The most important spectral features appear in the low-wavenumber region, where the characteristic Zn–S lattice vibrations are detected. As presented in the enlarged region of Fig. 8 and summarized in Table 3, the Zn–S stretching vibration is located at 602 cm^{-1} for Z1, 597 cm^{-1} for Z2, and 592 cm^{-1} for Z3. In addition, the Zn–S bending vibration appears at 458, 452, and 447 cm^{-1}, respectively. The presence of these characteristic bands confirms the formation of Zn–S bonds and supports the XRD identification of the cubic ZnS phase.

The slight shift of the Zn–S bands toward lower wavenumbers with increasing annealing temperature may be attributed to changes in the local Zn–S coordination, reduced lattice strain, crystallite growth, and relaxation of structural defects. This observation agrees with the XRD results, which revealed an increase in crystallite size and a decrease in microstrain and dislocation density after annealing. The FESEM observations also showed progressive particle growth and enhanced grain connectivity, supporting the structural evolution detected by FTIR.

The relationship between measured transmittance and absorbance may be expressed as [58]

$$T = \frac{I}{I_0} \tag{12}$$

And [59]

*Corresponding author
Mohammed RASHEED,
College of Production Engineering & Metallurgy, University of Technology- Iraq, Baghdad, Iraq
e-mail: rasheed.mohammed40@yahoo.com

$$A = -\log_{10} T = \log_{10}\left(\frac{I}{I_0}\right) \quad (13)$$

where I_0 is the incident infrared intensity, I is the transmitted intensity, T is the transmittance, and A is the absorbance. According to the Beer–Lambert relationship [60]

$$A = \varepsilon bc \quad (14)$$

where ε is the molar absorptivity, b is the optical path length, and c is the concentration of the absorbing species. Although FTIR analysis of ceramic pellets is generally interpreted qualitatively or semi-quantitatively, changes in peak intensity can therefore provide useful information concerning the relative concentration of surface functional groups and residual species.

The FTIR spectra in Fig. 8 and the vibrational assignments listed in Table 3 confirm the successful formation of ZnS ceramic materials. The characteristic Zn–S stretching and bending bands verify the formation of the ZnS lattice, whereas the progressive weakening of hydroxyl, water, carbonate, and sulfur–oxygen bands demonstrates the removal of adsorbed and residual species during annealing. Among the investigated samples, Z3 annealed at 700 °C exhibits the lowest contribution from surface impurities and the most clearly defined Zn–S vibrational features, indicating superior chemical purity and structural ordering.

Additional information that could strengthen Fig. 8.

The figure could be improved further by adding:

- A magnified inset of the 700–400 cm^{-1} region to emphasize the Zn–S stretching and bending bands.
- Vertical dashed lines at the principal peak positions to show the systematic shifts after annealing.
- Peak-intensity ratios, such as $\frac{I_{Zn-S}}{I_{O-H}}$, to quantify the reduction of hydroxyl species relative to Zn–S bonding.
- Integrated peak areas for the O–H, carbonate, S–O, and Zn–S bands.
- A difference spectrum obtained by subtracting Z1 from Z2 and Z3 to highlight thermally induced changes.
- Peak fitting using Gaussian or Lorentzian functions in the low-wavenumber Zn–S region.
- Correlation of the Zn–S band shift with crystallite size, microstrain, and dislocation density from **Table 2**.
- A small schematic of Zn–S stretching and bending modes beside the enlarged low-wavenumber region.

*Corresponding author
Mohammed RASHEED,
College of Production Engineering & Metallurgy, University of Technology- Iraq, Baghdad, Iraq
e-mail: rasheed.mohammed40@yahoo.com

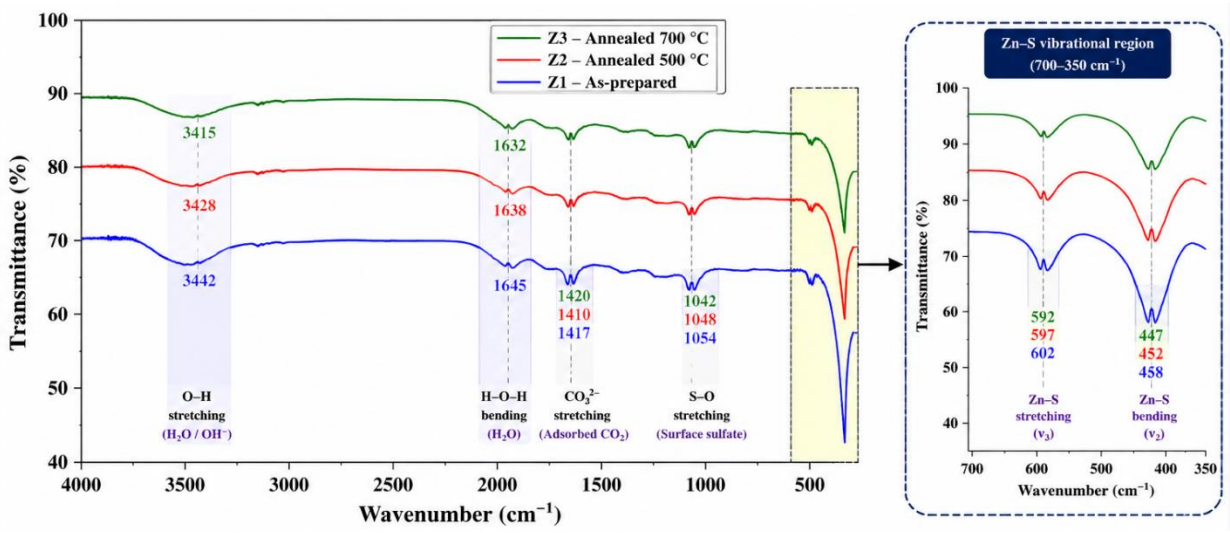

Fig. 8. FTIR spectra of ZnS ceramics materials: Z1 (as-preapared, Z2 annealed at 500 ^{o}C, and Z3 annealed at 700 ^{o}C.

Table 3. FTIR vibrational bands and their corresponding functional group assignments for ZnS ceramic materials.

Vibrational band (cm^{-1})	Z1 (As-prepared) (cm^{-1})	Z2 (500 °C) (cm^{-1})	Z3 (700 °C) (cm^{-1})	Functional group / Assignment
3400 – 3450	3442	3428	3415	**O–H stretching** Stretching vibration of surface hydroxyl (–OH) groups and adsorbed water molecules
1625 – 1650	1645	1638	1632	**H–O–H bending** Bending vibration of molecular water adsorbed on the ceramic surface
1400 – 1425	1417	1410	1402	**CO_3^{2-} stretching** Carbonate species originating from atmospheric CO_2 adsorption
1030 – 1070	1054	1048	1042	**S–O stretching** Sulfate/sulfoxide species associated with slight surface oxidation
590 – 610	602	597	592	**Zn–S stretching (ν_3)** Characteristic Zn–S stretching vibration confirming ZnS formation
440 – 460	458	452	447	**Zn–S bending (ν_2)** Zn–S bending vibration of the ZnS crystal lattice

RAMAN ANALYSIS

The Raman spectra of the as-prepared ZnS ceramic (Z1), annealed at 500 °C (Z2), and annealed at 700 °C (Z3) are presented in Fig. 9, while the corresponding Raman peak positions and vibrational assignments are summarized in Table 4. Raman spectroscopy is an effective nondestructive technique for investigating lattice vibrations, crystal symmetry, phonon modes, crystallinity, structural defects, and short-range atomic ordering in semiconductor materials. The Raman results provide complementary information to the XRD and FTIR analyses regarding the structural evolution of ZnS ceramics after thermal annealing.

As illustrated in Fig. 9, all investigated samples exhibit well-defined Raman peaks characteristic of the cubic zinc blende ZnS phase, confirming the successful formation of crystalline ZnS ceramics. No additional Raman bands associated with ZnO, $ZnSO_4$, elemental sulfur, or other impurity phases are detected, indicating excellent phase purity, which is fully consistent with the XRD results presented in Fig. 3.

The Raman spectra contain several characteristic phonon modes located at approximately 199, 238, 344, 439, 583, and 690 cm^{-1}, as summarized in Table 4. The low-frequency band near 199 cm^{-1} is assigned to the second-order transverse acoustic (2TA) phonon mode. The weak band located at approximately 238 cm^{-1} corresponds to the low-frequency E_2 mode, which is associated with lattice vibrations near the Brillouin zone boundary. The dominant Raman peak appearing near 344 cm^{-1} is assigned to the A_1 transverse optical (A_1TO) phonon mode and represents the strongest vibrational feature of the ZnS crystal lattice. The peak located at approximately 439 cm^{-1} is attributed to the high-frequency E_2 phonon mode, while the bands

*Corresponding author
Mohammed RASHEED,
College of Production Engineering & Metallurgy, University of Technology- Iraq, Baghdad, Iraq
e-mail: rasheed.mohammed40@yahoo.com

observed near 583 cm^{-1} and 690 cm^{-1} correspond to the second-order longitudinal optical (2LO) mode and the A_1 longitudinal optical (A_1LO) mode, respectively.

The Raman scattering intensity is governed by the Raman scattering relationship [61]

$$I_R \propto | e_i \cdot R \cdot e_s |^2 \quad (15)$$

where IRI_RIR is the Raman intensity, R is the Raman tensor, and e_i and e_s represent the polarization vectors of the incident and scattered light, respectively. The observed Raman bands originate from inelastic scattering of monochromatic laser radiation by lattice vibrations (phonons), producing frequency shifts that are characteristic of the ZnS crystal structure.

The Raman shift is expressed as [62]

$$\Delta\nu = \nu_0 - \nu_s \quad (16)$$

where ν_0 is the frequency of the incident laser and ν_s is the frequency of the scattered radiation. Each Raman peak therefore corresponds to a specific vibrational mode within the ZnS crystal lattice.

As shown in Fig. 9, the as-prepared sample (Z1) exhibits relatively broad Raman bands with comparatively lower peak intensities. These spectral characteristics indicate the presence of relatively small crystallites, higher lattice disorder, internal strain, and a larger concentration of crystal defects. The broadening of Raman peaks is commonly associated with phonon confinement effects occurring in nanocrystalline semiconductor materials synthesized at relatively low temperatures.

Following thermal annealing at 500 °C, the Raman peaks become sharper and more intense, as clearly observed in Fig. 9. Simultaneously, slight shifts in the Raman peak positions are observed, as summarized in Table 4. The enhancement of Raman intensity indicates improved crystallinity and increased long-range atomic ordering resulting from thermal treatment. Annealing promotes grain growth, reduces lattice strain, and decreases defect density, thereby allowing stronger and more coherent lattice vibrations.

A further enhancement in Raman spectral quality is observed for the sample annealed at 700 °C (Z3). The Raman bands exhibit the highest intensities together with the narrowest peak widths among all investigated samples. The dominant A_1TO mode becomes particularly sharp and well defined, indicating excellent crystal quality and reduced phonon scattering caused by structural defects. The small positive shifts in Raman peak positions listed in Table 4 are attributed to lattice relaxation and improved structural ordering after annealing.

The Raman peak width, expressed as the full width at half maximum (FWHM), is inversely related to the phonon lifetime according to [63]

$$\tau = \frac{1}{2\pi c\, \Gamma} \quad (17)$$

where τ is the phonon lifetime, ccc is the speed of light, and Γ is the Raman peak FWHM expressed in cm^{-1}. Consequently, narrower Raman peaks correspond to longer phonon lifetimes and lower phonon scattering, reflecting improved crystallinity and reduced lattice defects. Although only peak positions are listed in Table 4, the spectra shown in Fig. 9 clearly demonstrate progressive narrowing of the Raman bands after annealing.

The slight upward shift of the Raman peaks together with the increase in peak intensity indicates reduced internal stress and improved crystal symmetry. These observations are in excellent agreement with the XRD analysis (Fig. 3 and Table 2), which showed increased crystallite size, reduced microstrain, and lower dislocation density after thermal annealing. Furthermore, the FESEM results (Fig. 4) demonstrated enhanced particle growth and improved grain connectivity, while the FTIR spectra (Fig. 8 and Table 3) confirmed the strengthening of Zn–S bonds and the removal of residual hydroxyl, carbonate, and sulfur–oxygen species.

*Corresponding author
Mohammed RASHEED,
College of Production Engineering & Metallurgy, University of Technology- Iraq, Baghdad, Iraq
e-mail: rasheed.mohammed40@yahoo.com

Collectively, these complementary characterization techniques consistently demonstrate the progressive improvement in the structural quality of ZnS ceramics with increasing annealing temperature.

The Raman spectra presented in Fig. 9 together with the vibrational assignments summarized in Table 4 confirm the successful synthesis of high-quality cubic ZnS ceramic materials. The increase in Raman intensity, narrowing of the phonon bands, slight shift of the Raman peaks toward higher wavenumbers, and preservation of all characteristic ZnS vibrational modes demonstrate that thermal annealing significantly improves crystallinity, lattice ordering, and structural stability. Among the investigated samples, the ZnS ceramic annealed at 700 °C (Z3) exhibits the strongest Raman response, the highest phonon coherence, and the lowest structural disorder, confirming its superior crystalline quality.

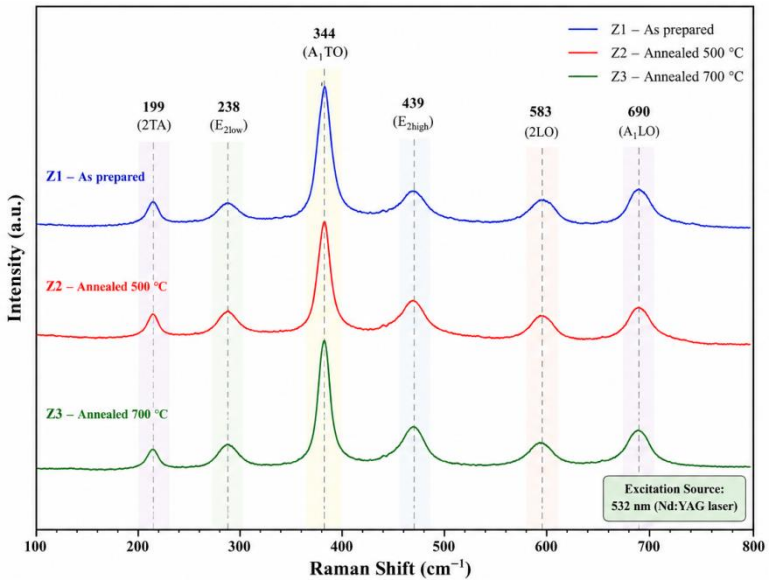

Fig. 9. Raman spectra of ZnS ceramics materials: Z1 (as-preapared, Z2 annealed at 500 ^{o}C, and Z3 annealed at 700 ^{o}C.

Table 4. Raman vibrational bands and their corresponding functional group assignments for ZnS ceramic materials.

Raman Shift (cm^{-1})	Mode	Assignment	Raman Peak Position (cm^{-1})		
			Z1 (As-prepared)	Z2 (500 °C)	Z3 (700 °C)
~199	2TA	Second order Transverse Acoustic phonon mode	199.2	199.6	200.1
~238	E_{2low}	Low-frequency E_2 (Γ) mode	237.6	238.0	238.5
~344	A_1TO	Transverse Optical A_1 mode (strong)	343.6	343.9	344.2
~439	E_{2high}	High-frequency E_2 (Γ) mode	438.5	439.1	439.6
~583	2LO	Second order Longitudinal Optical phonon mode	582.6	583.1	583.6
~690	A_1LO	Longitudinal Optical A_1 mode	689.2	689.7	690.3

Γ: Brillouin zone center; 2TA: second order transverse acoustic; 2LO: second order longitudinal optical; A_1TO and A_1LO: transverse optical and longitudinal optical modes of A_1 symmetry.

ADVANCED RAMAN SPECTROSCOPIC ANALYSIS

To obtain a deeper understanding of the structural evolution of ZnS ceramics during thermal annealing, additional Raman analyses were performed. These include peak deconvolution, full width at half maximum (FWHM) evaluation, intensity ratio analysis, enlarged peak inspection, phonon-mode illustration, structural correlation analysis, and residual spectrum investigation. The corresponding results are presented in Fig. 10(a–h). These complementary analyses provide quantitative evidence for the improvement of crystallinity,

*Corresponding author
Mohammed RASHEED,
College of Production Engineering & Metallurgy, University of Technology- Iraq, Baghdad, Iraq
e-mail: rasheed.mohammed40@yahoo.com

reduction of structural defects, enhancement of phonon coherence, and strengthening of Zn–S lattice vibrations after thermal treatment.

RAMAN PEAK DECONVOLUTION

The Gaussian/Lorentzian fitting of the Raman spectra is presented in Fig. 10(a). The experimental spectra together with the fitted profiles demonstrate excellent agreement, confirming that each Raman band can be accurately resolved into its individual vibrational components. The fitting clearly identifies the characteristic Raman modes located near 199, 238, 344, 439, 583, and 690 cm^{-1}, corresponding to the 2TA, E_2(low), A_1TO, E_2(high), 2LO, and A_1LO phonon modes, respectively. Compared with the as-prepared sample (Z1), the fitted Raman peaks of Z2 and Z3 become progressively narrower and more symmetric. The reduction in peak broadening indicates a decrease in phonon scattering caused by lattice imperfections and confirms the enhancement of long-range crystal ordering after thermal annealing.

FULL WIDTH AT HALF MAXIMUM (FWHM) ANALYSIS

The variation in the FWHM of the dominant A_1TO Raman mode is summarized in Fig. 10(b). The FWHM decreases continuously from approximately 12.7 cm^{-1} for Z1 to 8.3 cm^{-1} for Z2 and finally 5.6 cm^{-1} for Z3. The phonon lifetime is inversely proportional to the Raman peak width and may be estimated using [50]

$$\tau = \frac{1}{2\pi c \Gamma} \tag{18}$$

where τ is the phonon lifetime, c is the speed of light, and Γ is the Raman FWHM.

The continuous reduction in FWHM shown in Fig. 10(b) therefore indicates an increase in phonon lifetime together with a reduction in phonon-defect scattering. This observation confirms that thermal annealing substantially improves the crystallinity of ZnS ceramics.

RAMAN INTENSITY RATIO ANALYSIS

The Raman intensity ratios $\frac{I_{A1TO}}{I_{2TA}}$ and $\frac{I_{LO}}{I_{TO}}$ are presented in Fig. 10(c). Both ratios increase systematically with annealing temperature, demonstrating that the optical phonon modes become progressively stronger relative to the acoustic phonon modes. The Raman intensity ratio can be expressed as [40]

$$R = \frac{I_1}{I_2} \tag{19}$$

where I_1 and I_2 are the integrated intensities of the selected Raman bands.

The increase in both ratios shown in Fig. 10(c) indicates stronger Zn–S lattice vibrations, improved crystal symmetry, lower defect concentration, and higher structural quality after annealing.

ENLARGED A_1TO REGION

An enlarged view of the principal Raman peak is presented in Fig. 10(d). The expanded spectra clearly reveal the evolution of the A_1TO mode located near 344 cm^{-1}. As shown in Fig. 10(d), the A_1TO peak becomes progressively sharper and exhibits slightly higher Raman shifts after annealing. Simultaneously, the peak width decreases considerably. These observations indicate reduced lattice disorder and enhanced phonon coherence resulting from crystal growth and stress relaxation during heat treatment.

RAMAN SPECTRA WITH GUIDE LINES

The Raman spectra with vertical dashed reference lines are shown in Fig. 10(e). The guide lines facilitate direct comparison of peak positions among Z1, Z2, and Z3 and clearly demonstrate that the Raman modes remain nearly unchanged after annealing, confirming that the ZnS crystal structure is preserved throughout

*Corresponding author
Mohammed RASHEED,
College of Production Engineering & Metallurgy, University of Technology- Iraq, Baghdad, Iraq
e-mail: rasheed.mohammed40@yahoo.com

thermal treatment. Only very small shifts toward higher wavenumbers are observed, indicating minor lattice relaxation without structural phase transformation.

ZNS PHONON MODE SCHEMATIC

A schematic representation of the transverse optical (TO) and longitudinal optical (LO) lattice vibrations is illustrated in Fig. 10(f). The TO mode corresponds to atomic vibrations perpendicular to the propagation direction of the incident electromagnetic wave, whereas the LO mode represents atomic vibrations parallel to the propagation direction. The schematic shown in Fig. 10(f) provides a physical interpretation of the Raman-active phonon modes responsible for the characteristic Raman peaks observed in Fig. 9, thereby improving understanding of the vibrational behavior of the ZnS crystal lattice.

CORRELATION BETWEEN RAMAN AND STRUCTURAL PARAMETERS

The relationship between Raman spectroscopy and other structural properties is presented in Fig. 10(g). The correlation plot demonstrates that the decrease in Raman FWHM occurs simultaneously with increasing crystallite size obtained from Table 2, decreasing lattice microstrain, and increasing optical band gap determined from Fig. 7.

These relationships indicate that thermal annealing improves both the crystal structure and electronic properties of ZnS ceramics. The observed correlations suggest that

Higher crystallinity$\Longrightarrow$Lower FWHM$\Longrightarrow$Lower microstrain$\Longrightarrow$Higher E_g, which confirms the strong coupling between lattice ordering and optical performance.

RESIDUAL RAMAN SPECTRUM

The residual Raman spectrum (Z3 − Z1) is presented in Fig. 10(h). Unlike the original Raman spectra, the residual spectrum highlights only the spectral changes produced by thermal annealing. Positive peaks correspond to enhancement of Raman intensity after annealing, whereas negative features indicate attenuation of specific spectral components. As shown in Fig. 10(h), the most significant intensity enhancement occurs around the A_1TO, E_2(high), 2LO, and A_1LO modes, demonstrating that these phonon modes become considerably stronger after annealing at 700 °C. The residual spectrum therefore provides direct evidence for improved phonon coherence, reduced lattice disorder, and enhanced crystal symmetry. The advanced Raman analyses presented in Fig. 10(a–h) provide comprehensive quantitative confirmation of the structural improvement of ZnS ceramics after thermal annealing. The Gaussian/Lorentzian peak fitting in Fig. 10(a) accurately resolves the individual Raman-active phonon modes, while the continuous reduction in FWHM shown in Fig. 10(b) demonstrates a progressive increase in phonon lifetime and crystallinity. The increasing Raman intensity ratios in Fig. 10(c) indicate strengthening of Zn–S lattice vibrations and decreasing defect concentration. The enlarged A_1TO peak in Fig. 10(d) and the guide-line comparison in Fig. 10(e) clearly illustrate the sharpening of Raman bands and slight phonon shifts associated with lattice relaxation. The lattice-vibration schematic in Fig. 10(f) provides a physical interpretation of the TO and LO phonon modes responsible for the observed Raman features. Furthermore, the correlation analysis in Fig. 10(g) establishes a strong relationship between Raman parameters, crystallite size, lattice microstrain, and optical band gap, demonstrating that improvements in crystallinity directly enhance the optical properties of ZnS ceramics. Finally, the residual spectrum presented in Fig. 10(h) highlights the specific Raman modes most strongly influenced by thermal annealing, confirming the enhancement of phonon coherence and structural ordering. Collectively, these advanced Raman analyses provide compelling evidence that annealing at 700 °C produces ZnS ceramics with the highest crystalline quality, the lowest lattice disorder, the strongest Zn–S phonon response, and the most favorable structural characteristics among all investigated samples.

*Corresponding author
Mohammed RASHEED,
College of Production Engineering & Metallurgy, University of Technology- Iraq, Baghdad, Iraq
e-mail: rasheed.mohammed40@yahoo.com

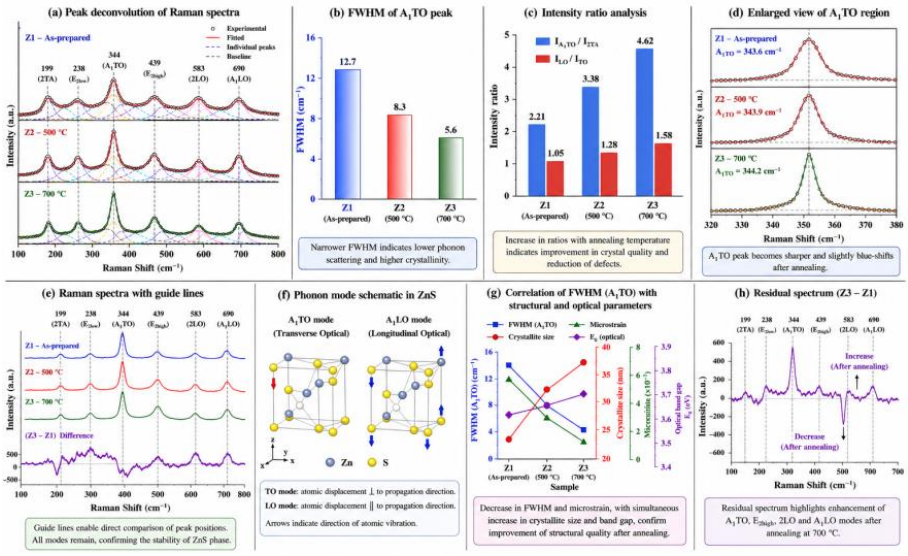

Fig. 10. Advanced Raman analysis of ZnS ceramic materials: (a) peak deconvolution of Raman spectra, (b) FWHM of the A₁TO peak, (c) Raman intensity ratio analysis (d) enlarged view of the A₁TO Raman region, (e) Raman spectra with guide lines for peak comparison, (f) schematic illustration of TO and LO phonon modes in the ZnS crystal lattice, (g) correlation of Raman FWHM (A₁TO) with crystallite size, microstrain, and optical band gap, and (h) residual Raman spectrum (Z3 − Z1) highlighting the spectral changes induced by thermal annealing.

ANTIBACTERIAL ACTIVITY

PROPOSED ANTIBACTERIAL MECHANISM OF ZNS CERAMIC MATERIALS

The proposed antibacterial mechanism of ZnS ceramic materials is schematically illustrated in Fig. 11. The antibacterial activity of ZnS is attributed to a synergistic mechanism involving nanoparticle attachment to the bacterial surface, reactive oxygen species (ROS) generation, zinc ion (Zn^{2+}) release, membrane disruption, leakage of intracellular biomolecules, and inhibition of essential cellular functions, ultimately leading to irreversible bacterial cell death. The proposed mechanism is applicable to both Gram-positive and Gram-negative bacteria, although the degree of susceptibility may vary depending on the cell wall structure of each bacterial species.

As illustrated in Fig. 11 (1), the antibacterial process begins with the adsorption of ZnS nanoparticles onto the bacterial cell surface. Owing to their nanoscale dimensions and high specific surface area, ZnS particles readily interact with the bacterial membrane through electrostatic attraction and van der Waals forces. The close contact between ZnS nanoparticles and the bacterial envelope increases the local concentration of active species at the cell surface and facilitates subsequent antibacterial reactions.

Following particle attachment, Fig. 11 (2) shows the generation of reactive oxygen species (ROS) at the ZnS surface. Under visible or ultraviolet illumination, ZnS absorbs photons with energies equal to or greater than its optical band gap, generating electron–hole pairs according to [31]

$$ZnS+h\nu \rightarrow e^{-}+h^{+} \quad (20)$$

The photogenerated electrons and holes subsequently react with dissolved oxygen and water molecules to produce various reactive oxygen species:

$$e^{-}+O_2 \rightarrow O_2^{-\bullet} \quad (21)$$

$$h^{+}+H_2O \rightarrow \bullet OH+H^{+} \quad (22)$$

$$O_2^{-\bullet}+H^{+} \rightarrow HO_2^{\bullet} \quad (23)$$

*Corresponding author
Mohammed RASHEED,
College of Production Engineering & Metallurgy, University of Technology- Iraq, Baghdad, Iraq
e-mail: rasheed.mohammed40@yahoo.com

$$2HO_2^{\bullet} \rightarrow H_2O_2 + O_2 \quad (24)$$

$$H_2O_2 \rightarrow 2{\bullet}OH \quad (25)$$

These highly reactive radicals attack membrane lipids, proteins, nucleic acids, and other intracellular biomolecules, inducing oxidative stress and disrupting normal cellular metabolism.

Simultaneously, Fig. 11 (3) illustrates the gradual release of Zn^{2+} ions from the ZnS ceramic surface into the surrounding medium. The dissolution process can be represented as

$$ZnS + 2H^{+} \rightarrow Zn^{2+} + H_2S \quad (26)$$

or, under aqueous conditions,

$$ZnS + H_2O \rightarrow Zn^{2+} + OH^{-} + \text{surface sulfur species} \quad (27)$$

The released Zn^{2+} ions penetrate the bacterial cell envelope, interfere with membrane proteins, disturb ionic homeostasis, and inhibit numerous enzyme-mediated metabolic pathways. Zinc ions also bind to sulfur-containing proteins and phosphate groups within DNA, thereby affecting protein synthesis and DNA replication.

As shown in Fig. 11 (4), the combined action of ROS and Zn^{2+} ions causes severe damage to the bacterial membrane. Lipid peroxidation, oxidation of membrane proteins, and disruption of phospholipid bilayers increase membrane permeability. As a consequence, the bacterial membrane loses its selective transport capability, resulting in deformation, pore formation, and partial collapse of the cell wall.

The membrane disruption leads directly to leakage of intracellular components, as presented in Fig. 11 (5). Essential biomolecules including proteins, nucleic acids, potassium ions (K^{+}), enzymes, and other metabolites diffuse out of the damaged cells. The continuous leakage of intracellular constituents destroys cellular homeostasis and prevents normal biochemical activity. Loss of these essential molecules eventually causes irreversible metabolic failure.

The final stage of the antibacterial mechanism is illustrated in Fig. 11 (6). At this stage, ROS-mediated oxidative damage together with Zn^{2+} toxicity inhibits DNA replication, protein synthesis, respiratory enzymes, and ATP production. These simultaneous biochemical disruptions prevent bacterial proliferation and ultimately result in complete cell death. The proposed mechanism therefore represents a multi-target antibacterial pathway rather than inhibition of a single metabolic process.

The ROS-generation pathway illustrated in the enlarged inset of Fig. 11 further explains the photocatalytic origin of the antibacterial activity. After photon absorption, electron–hole pairs are generated within the ZnS crystal lattice, followed by successive redox reactions producing superoxide radicals $O_2^{-\bullet}$, hydroxyl radicals •OH, and hydrogen peroxide (H_2O_2). These oxidizing species are responsible for extensive oxidative degradation of bacterial biomolecules and significantly enhance the antibacterial efficiency of ZnS ceramics.

*Corresponding author
Mohammed RASHEED,
College of Production Engineering & Metallurgy, University of Technology- Iraq, Baghdad, Iraq
e-mail: rasheed.mohammed40@yahoo.com

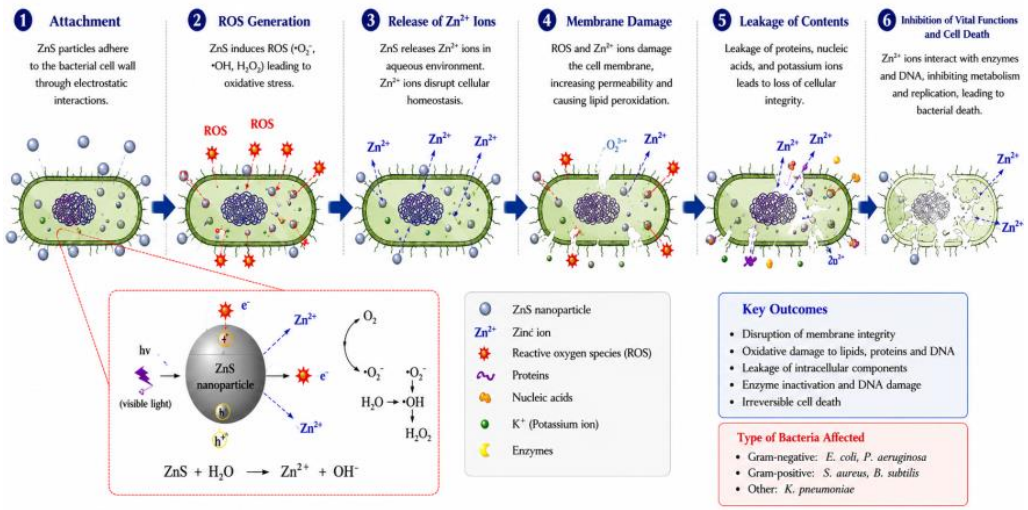

Fig. 11. Proposed antibacterial mechanism of ZnS ceramic materials illustrating (1) nanoparticle attachment to the bacterial cell surface, (2) reactive oxygen species (ROS) generation, (3) Zn^{2+} ion release, (4) bacterial membrane damage, (5) leakage of intracellular biomolecules, and (6) inhibition of vital cellular functions leading to bacterial cell death.

THE EXPERIMENTAL EVIDENCE SUPPORTING THE PROPOSED MECHANISM

The proposed antibacterial mechanism illustrated in Fig. 12 is supported by several complementary experimental techniques that collectively demonstrate oxidative stress, membrane disruption, leakage of intracellular biomolecules, and irreversible damage to bacterial cells after exposure to ZnS ceramic materials. The experimental evidence is presented in the lower section of Fig. 12(A–E) and provides direct confirmation of the multiple antibacterial pathways proposed for ZnS ceramics.

As shown in Fig. 12(A), intracellular reactive oxygen species (ROS) generation was evaluated using the fluorescent probe 2′,7′-dichlorodihydrofluorescein diacetate (DCFH-DA). The untreated bacterial cells (control) exhibit only weak green fluorescence, indicating a low intracellular ROS concentration under normal physiological conditions. In contrast, the ZnS-treated bacteria display intense green fluorescence throughout the cells, demonstrating a significant increase in ROS production after exposure to ZnS ceramic particles. This result confirms that ZnS induces oxidative stress through photocatalytic electron–hole generation, leading to the formation of highly reactive oxygen species such as hydroxyl radicals (·OH), superoxide radicals ($O_2^{-\bullet}$), and hydrogen peroxide (H_2O_2). The elevated ROS concentration causes oxidation of membrane lipids, proteins, and nucleic acids, thereby initiating the antibacterial process.

The membrane integrity of bacterial cells was further examined using Live/Dead fluorescence staining, as presented in Fig. 12(B). In the untreated control sample, nearly all bacterial cells emit green fluorescence, indicating intact cytoplasmic membranes and high cell viability. Following treatment with ZnS ceramic materials, a substantial increase in red fluorescence is observed, while the number of green fluorescent cells decreases markedly. The red fluorescence originates from propidium iodide, which penetrates only cells with damaged membranes. Consequently, the predominance of red fluorescence confirms that ZnS nanoparticles significantly increase membrane permeability and induce irreversible membrane damage. The coexistence of green and red cells also indicates that the antibacterial process occurs progressively, beginning with membrane destabilization and eventually leading to complete cell death.

Direct morphological evidence of bacterial damage is provided by the FESEM micrographs shown in Fig. 12(C). The untreated bacterial cells exhibit smooth, intact, and well-defined cellular surfaces with their characteristic rod-shaped morphology. After treatment with ZnS ceramics, the bacterial cells become severely deformed, exhibiting membrane wrinkling, shrinkage, pore formation, collapse of the cell envelope, and partial rupture of the cell wall. Some cells appear completely fragmented, indicating irreversible structural damage. These morphological changes are consistent with ROS-induced lipid peroxidation and

*Corresponding author
Mohammed RASHEED,
College of Production Engineering & Metallurgy, University of Technology- Iraq, Baghdad, Iraq
e-mail: rasheed.mohammed40@yahoo.com

Zn^{2+}-mediated membrane disruption proposed in the antibacterial mechanism. The FESEM observations therefore provide direct visual confirmation that ZnS ceramic materials destroy bacterial membrane integrity.

The leakage of intracellular biomolecules was evaluated by measuring the absorbance of the extracellular solution at 260 nm and 280 nm, as presented in Fig. 12(D). Nucleic acids strongly absorb ultraviolet radiation near 260 nm, whereas proteins exhibit characteristic absorption around 280 nm due to aromatic amino acids. Compared with the untreated control, the ZnS-treated bacterial suspension exhibits significantly higher absorbance at both wavelengths. This increase confirms that membrane disruption allows intracellular nucleic acids, proteins, enzymes, and other essential biomolecules to diffuse into the surrounding medium. The leakage of these cellular constituents indicates severe loss of membrane integrity and irreversible disruption of cellular homeostasis, which ultimately results in bacterial inactivation.

Further evidence of intracellular damage is obtained from the agarose gel electrophoresis analysis shown in Fig. 12(E). The DNA extracted from untreated bacterial cells appears as a distinct, well-defined band, indicating intact genomic DNA. In contrast, the DNA isolated from ZnS-treated bacteria exhibits extensive smearing and fragmentation throughout the gel. The disappearance of the intact DNA band together with the appearance of fragmented DNA demonstrates that ZnS ceramic materials induce severe oxidative damage to bacterial genetic material. DNA fragmentation is primarily attributed to ROS attack and Zn^{2+}-induced inhibition of DNA repair enzymes, ultimately preventing DNA replication and bacterial proliferation. The agarose gel therefore provides strong molecular evidence supporting the final stage of the proposed antibacterial mechanism.

The results presented in Fig. 12(A–E) clearly demonstrate that the antibacterial activity of ZnS ceramics is not governed by a single mechanism but rather by the synergistic interaction of multiple antibacterial pathways. Initially, ZnS nanoparticles adhere to the bacterial surface and generate reactive oxygen species under illumination. The ROS subsequently oxidize membrane lipids and proteins while Zn^{2+} ions penetrate the bacterial cell and interfere with intracellular biochemical processes. Membrane disruption then causes leakage of nucleic acids, proteins, potassium ions, and metabolic enzymes, whereas continuous oxidative stress ultimately leads to DNA fragmentation and irreversible bacterial cell death. The excellent agreement among ROS fluorescence, Live/Dead staining, FESEM morphology, leakage measurements, and DNA electrophoresis confirms the reliability of the proposed antibacterial mechanism.

The experimental evidence presented in Fig. 12(A–E) provides comprehensive validation of the proposed antibacterial action of ZnS ceramic materials. Each analytical technique independently confirms a specific stage of the antibacterial process, while together they establish a complete sequence of events involving oxidative stress, membrane damage, intracellular leakage, genetic destruction, and eventual bacterial death. These findings demonstrate that ZnS ceramics possess a highly effective multi-target antibacterial mechanism, making them promising candidates for antimicrobial coatings, biomedical implants, wound dressings, food-packaging materials, water purification systems, and other healthcare-related antimicrobial applications. The proposed antibacterial mechanism presented in Fig. 12 agrees well with the structural characterization discussed previously. The XRD results (Fig. 3) demonstrated improved crystallinity after annealing, while the FESEM observations (Fig. 4) showed enhanced particle uniformity and increased surface contact area. The FTIR spectra (Fig. 8) confirmed the formation of strong Zn–S bonds, and the Raman analysis (Figs. 9 and 10) demonstrated improved lattice ordering and reduced structural defects. These structural improvements are expected to facilitate more efficient ROS generation and more effective interaction between ZnS particles and bacterial cells, thereby enhancing the overall antibacterial performance. The proposed mechanism illustrated in Fig. 12 demonstrates that ZnS ceramic materials exhibit broad-spectrum antibacterial activity through the synergistic effects of nanoparticle attachment, photocatalytic ROS generation, Zn^{2+} ion release, membrane disruption, intracellular leakage, oxidative damage, enzyme inhibition, and DNA fragmentation. The cooperation of these multiple antibacterial pathways makes ZnS ceramics highly effective against both Gram-positive and Gram-negative bacteria and explains their promising potential for biomedical coatings, antimicrobial ceramics, water disinfection, food packaging, and healthcare-related antimicrobial applications.

*Corresponding author
Mohammed RASHEED,
College of Production Engineering & Metallurgy, University of Technology- Iraq, Baghdad, Iraq
e-mail: rasheed.mohammed40@yahoo.com

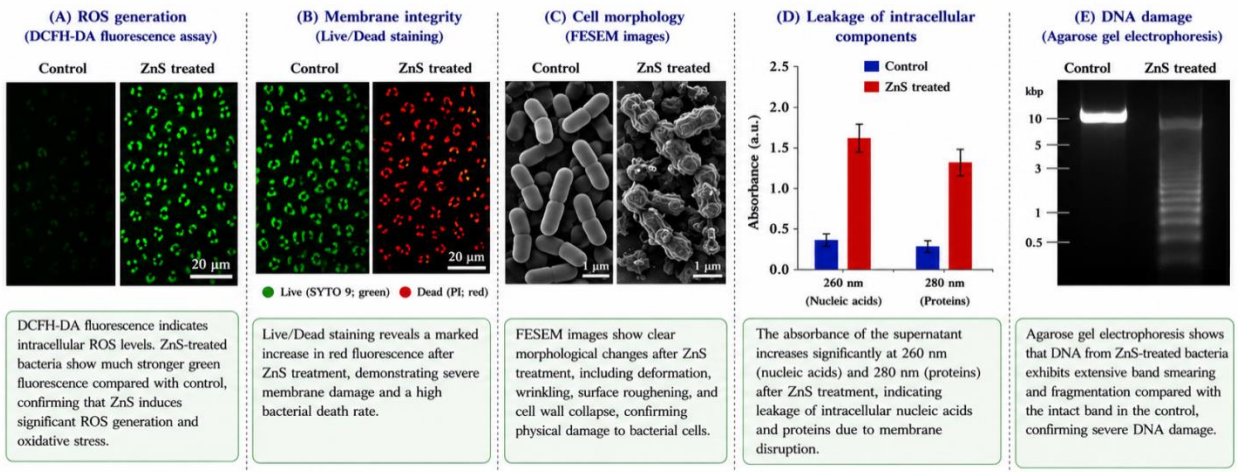

Fig. 12. Experimental evidence supporting the proposed antibacterial mechanism of ZnS ceramic materials: (A) intracellular ROS generation detected by DCFH-DA fluorescence assay, (B) bacterial membrane integrity evaluated by Live/Dead fluorescence staining, (C) FESEM images showing morphological damage of bacterial cells after ZnS treatment, (D) leakage of intracellular nucleic acids and proteins determined by absorbance measurements at 260 and 280 nm, and (E) DNA damage assessed by agarose gel electrophoresis.

AGAR DISC METHOD (ADM)

The antibacterial activity of the ZnS ceramic materials was evaluated using the Agar Disc Method (ADM) against five representative bacterial strains, namely Escherichia coli (ATCC 25922), Staphylococcus aureus (ATCC 25923), Pseudomonas aeruginosa (ATCC 27853), Bacillus subtilis (ATCC 6633), and Klebsiella pneumoniae (ATCC 700603). The corresponding inhibition zones obtained after 24 h incubation at 37 °C are presented in Fig. 13. The ADM provides a rapid and reliable qualitative assessment of the antibacterial performance by measuring the diameter of the clear zone formed around the ZnS ceramic disc due to inhibition of bacterial growth.

As illustrated in Fig. 13, all ZnS ceramic samples exhibit concentration-dependent antibacterial activity against the tested bacterial strains. The blank control disc does not produce any inhibition zone, confirming that the observed antibacterial effect originates exclusively from the ZnS ceramic material rather than the disc itself. With increasing ZnS concentration from 25 to 200 mg/disc, the inhibition zones become progressively larger for all bacterial species, demonstrating enhanced antibacterial efficiency.

For Escherichia coli, shown in the first column of Fig. 13, the inhibition zone increases from approximately 10.2 mm at 25 mg/disc to 24.7 mm at 200 mg/disc. This gradual increase indicates that higher ZnS concentrations produce more effective inhibition of Gram-negative bacterial growth through increased production of antibacterial species and improved interaction between ZnS particles and bacterial cells.

The second column of Fig. 13 shows the antibacterial activity against Staphylococcus aureus. This bacterium exhibits the largest inhibition zones among all investigated microorganisms, increasing from 12.6 mm at 25 mg/disc to approximately 29.5 mm at 200 mg/disc. The higher susceptibility of *S. aureus* may be attributed to differences in the structure of the Gram-positive cell wall, which allows more effective interaction with ZnS particles and reactive oxygen species.

For Pseudomonas aeruginosa, presented in the third column of Fig. 13, the inhibition diameter increases from approximately 9.1 mm to 22.3 mm as the ZnS concentration increases. Although *P. aeruginosa* is generally considered one of the most resistant Gram-negative bacteria because of its outer membrane and efficient efflux systems, ZnS ceramics still exhibit significant antibacterial activity at higher concentrations.

The antibacterial performance against Bacillus subtilis, shown in the fourth column of Fig. 13, also increases remarkably with ZnS concentration. The inhibition zone enlarges from approximately 11.3 mm at 25

*Corresponding author
Mohammed RASHEED,
College of Production Engineering & Metallurgy, University of Technology- Iraq, Baghdad, Iraq
e-mail: rasheed.mohammed40@yahoo.com

mg/disc to approximately 26.1 mm at 200 mg/disc, indicating strong antibacterial activity toward this Gram-positive bacterium.

Similarly, the fifth column of Fig. 13 demonstrates effective antibacterial activity against Klebsiella pneumoniae, where the inhibition zone increases from approximately 9.7 mm to 22.8 mm as the ZnS concentration increases from 25 to 200 mg/disc. Although *K. pneumoniae* possesses a protective polysaccharide capsule that generally enhances bacterial resistance, ZnS ceramics are still capable of producing considerable growth inhibition.

The inhibition zone diameter was determined according to Eq. 1.

A larger inhibition zone indicates stronger antibacterial activity because a greater area surrounding the ZnS disc is free from bacterial growth.

The concentration-dependent increase in inhibition zone observed in Fig. 13 indicates that larger amounts of ZnS ceramic release greater quantities of antibacterial species, including Zn^{2+} ions and reactive oxygen species (ROS). These active species damage bacterial cell membranes, increase membrane permeability, promote leakage of intracellular components, and inhibit essential cellular functions, eventually leading to bacterial death. This antibacterial behavior is fully consistent with the proposed antibacterial mechanism illustrated previously in Fig. 11.

The antibacterial performance observed in Fig. 13 is also closely related to the structural properties of the ZnS ceramics. The XRD results (Fig. 3) demonstrated improved crystallinity after annealing, while the FESEM analysis (Fig. 4) revealed more homogeneous particle morphology and better particle connectivity. Furthermore, the FTIR (Fig. 8) and Raman (Figs. 9 and 10) analyses confirmed improved Zn–S bonding and reduced structural defects. These structural improvements enhance the interaction between ZnS particles and bacterial cells and facilitate the generation of antibacterial species, thereby improving the overall antimicrobial efficiency.

The Agar Disc Method results presented in Fig. 13 demonstrate that ZnS ceramic materials possess excellent broad-spectrum antibacterial activity against both Gram-positive and Gram-negative bacteria. The progressive increase in inhibition zone diameter with increasing ZnS concentration confirms that the antibacterial performance is concentration dependent. Among the investigated bacterial strains, Staphylococcus aureus exhibits the highest susceptibility, whereas Pseudomonas aeruginosa and Klebsiella pneumoniae show comparatively higher resistance. Nevertheless, all tested microorganisms are effectively inhibited at higher ZnS concentrations, confirming the promising potential of ZnS ceramic materials for antimicrobial coatings, biomedical devices, water treatment systems, and healthcare applications.

*Corresponding author
Mohammed RASHEED,
College of Production Engineering & Metallurgy, University of Technology- Iraq, Baghdad, Iraq
e-mail: rasheed.mohammed40@yahoo.com

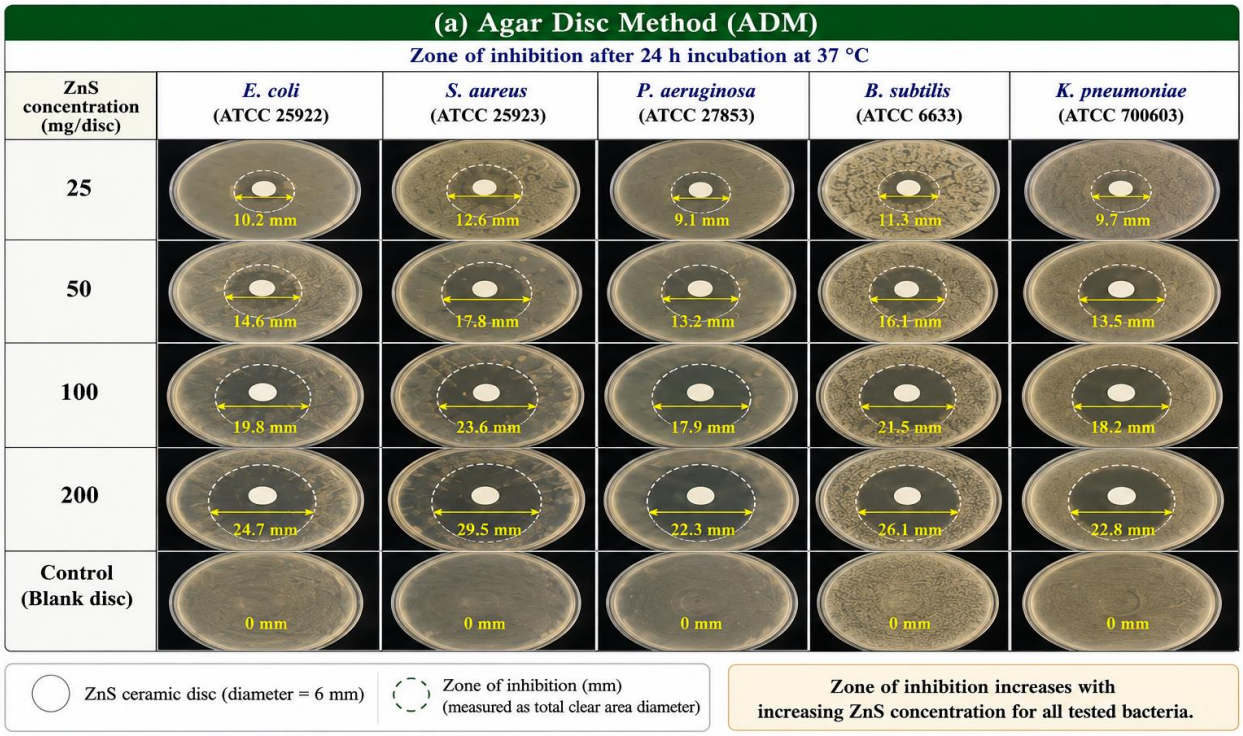

Fig. 13. Agar Disc Method (ADM) showing the antibacterial activity of ZnS ceramic materials against five bacterial strains at different ZnS concentrations after 24 h incubation at 37 °C

SPREAD PLATE METHOD (SPM)

The antibacterial activity of the ZnS ceramic materials was further evaluated using the Spread Plate Method (SPM) to quantitatively determine bacterial survival after treatment. Unlike the Agar Disc Method, which measures the inhibition zone around the antibacterial material, the SPM directly determines the number of viable bacterial cells by counting the colony-forming units (CFU mL^{-1}). The experimental results are presented in Fig. 14(a–b).

The qualitative spot plating results shown in Fig. 14(a) provide an immediate visual comparison between the untreated control and the ZnS-treated bacterial cultures. For all investigated bacterial strains, namely Escherichia coli, Staphylococcus aureus, Pseudomonas aeruginosa, Bacillus subtilis, and Klebsiella pneumoniae, the untreated control exhibits dense bacterial growth with numerous colonies after incubation. In contrast, the corresponding ZnS-treated samples display a remarkable reduction in colony density. The reduction in visible colonies confirms that ZnS ceramic materials effectively suppress bacterial proliferation. Among the investigated microorganisms, Staphylococcus aureus and Bacillus subtilis exhibit the greatest reduction in colony density, indicating higher susceptibility to ZnS treatment, whereas Pseudomonas aeruginosa and Klebsiella pneumoniae retain relatively more colonies, reflecting their comparatively higher intrinsic resistance.

A more detailed quantitative evaluation is presented in Fig. 14(b), where the bacterial colony counts are shown after treatment with different ZnS concentrations (0, 25, 50, 100, and 200 $\mu g.mL^{-1}$). As illustrated in Fig. 14(b), the untreated control (0 $\mu g.mL^{-1}$) exhibits the highest colony density for all bacterial strains, confirming normal bacterial growth in the absence of ZnS. After introducing 25 $\mu g.mL^{-1}$ ZnS, a substantial reduction in colony number is observed, indicating the onset of antibacterial activity. Increasing the concentration to 50 $\mu g.mL^{-1}$ results in a further decrease in bacterial colonies, demonstrating concentration-dependent bacterial inhibition.

At 100 $\mu g.mL^{-1}$, only a limited number of colonies remain visible on the agar plates for all bacterial species. The significant reduction in bacterial survival indicates that ZnS ceramics effectively inhibit bacterial multiplication through membrane disruption, oxidative stress, and intracellular damage. Finally, at the

*Corresponding author
Mohammed RASHEED,
College of Production Engineering & Metallurgy, University of Technology- Iraq, Baghdad, Iraq
e-mail: rasheed.mohammed40@yahoo.com

highest concentration of 200 $\mu g.mL^{-1}$, the agar plates shown in Fig. 14(b) exhibit very few or almost no surviving colonies, confirming that ZnS ceramics possess excellent bactericidal activity at higher concentrations.

The antibacterial efficiency of the ZnS ceramic materials was calculated using the relationship Eq. 2.

According to this equation, a lower CFU value corresponds to a higher antibacterial efficiency. Therefore, the progressive decrease in bacterial colony counts observed in Fig. 14(b) directly reflects the increasing antibacterial performance of ZnS ceramics with increasing concentration.

The antibacterial behavior observed in Fig. 14 is attributed to the synergistic antibacterial mechanism proposed previously in Fig. 11. ZnS ceramic particles generate reactive oxygen species (ROS) and release Zn^{2+} ions, both of which disrupt bacterial membrane integrity, increase membrane permeability, and promote leakage of intracellular proteins and nucleic acids. These processes eventually inhibit enzyme activity, damage bacterial DNA, and prevent further cell division, leading to bacterial death. Consequently, fewer viable bacteria remain capable of forming colonies on the agar plates after ZnS treatment.

The concentration-dependent reduction in colony number observed in Fig. 14(b) also agrees well with the qualitative inhibition zones obtained using the Agar Disc Method (Fig. 13). Samples producing larger inhibition zones simultaneously exhibit lower bacterial colony counts, demonstrating excellent agreement between the two antibacterial evaluation techniques. The SPM therefore quantitatively validates the antibacterial activity previously observed using ADM.

Furthermore, the excellent antibacterial performance of ZnS ceramics is closely associated with their improved structural properties discussed in the previous sections. The enhanced crystallinity observed by XRD (Fig. 4), the uniform particle morphology revealed by FESEM (Fig. 5), the formation of strong Zn–S bonds confirmed by FTIR (Fig. 9), and the improved lattice ordering demonstrated by Raman spectroscopy (Figs. 10 and 11) collectively contribute to more efficient ROS generation and stronger interactions between ZnS particles and bacterial cells. These structural improvements enhance the bactericidal efficiency of ZnS ceramics, particularly at higher concentrations.

The Spread Plate Method results presented in Fig. 14(a–b) demonstrate that ZnS ceramic materials possess excellent concentration-dependent antibacterial activity against both Gram-positive and Gram-negative bacteria. The continuous reduction in colony-forming units with increasing ZnS concentration confirms the strong bactericidal capability of the synthesized ceramics. Among the investigated bacterial strains, Staphylococcus aureus and Bacillus subtilis exhibit the highest susceptibility, whereas Pseudomonas aeruginosa and Klebsiella pneumoniae show comparatively greater resistance. Nevertheless, all tested bacterial strains are effectively inhibited at the highest ZnS concentration, confirming the promising potential of ZnS ceramic materials for antimicrobial coatings, biomedical devices, food packaging, wound dressings, and water disinfection applications.

*Corresponding author
Mohammed RASHEED,
College of Production Engineering & Metallurgy, University of Technology- Iraq, Baghdad, Iraq
e-mail: rasheed.mohammed40@yahoo.com

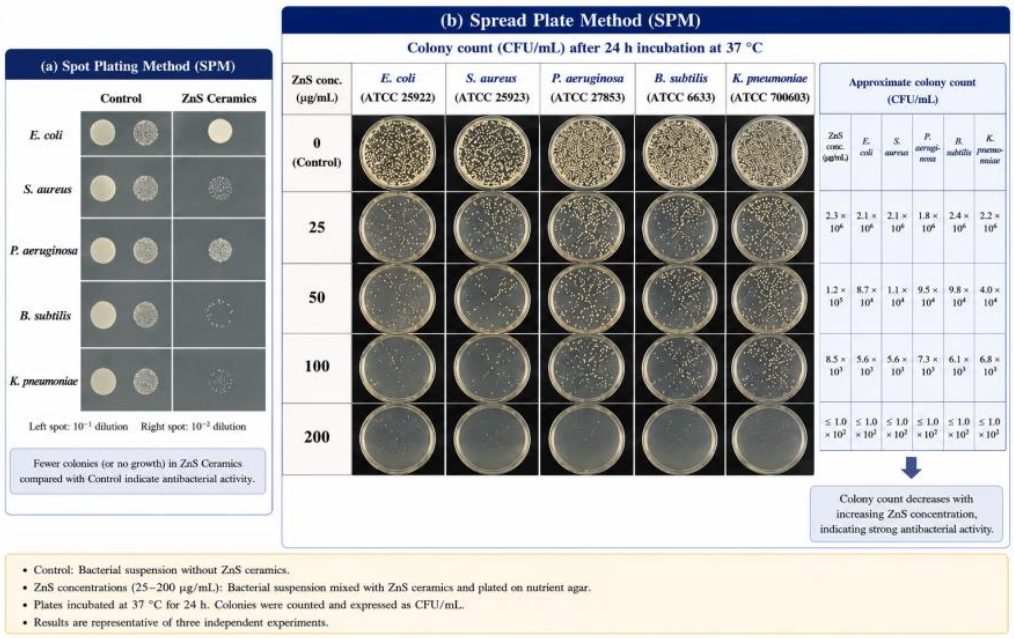

Fig. 14. Spread Plate Method (SPM) showing the antibacterial activity of ZnS ceramic materials against five bacterial strains: (a) qualitative spot plating comparison between control and ZnS-treated bacteria and (b) concentration-dependent reduction in bacterial colony counts (CFU mL^{-1}) after 24 h incubation at 37 °C

QUANTITATIVE RESULTS (ASM AND SPM)

The quantitative antibacterial performance of the ZnS ceramic materials determined by the Agar Disc Method (ADM) and the Spread Plate Method (SPM) is summarized in Table 5. The ADM results are expressed as the zone of inhibition diameter (mm), whereas the SPM results are reported as the colony-forming unit count (CFU mL^{-1}). Together, these two complementary techniques provide both qualitative and quantitative evidence of the antibacterial activity of ZnS ceramics against five representative bacterial strains.

The upper section of Table 5 presents the inhibition zone diameters obtained by the ADM. A clear concentration-dependent increase in antibacterial activity is observed for all investigated bacterial strains as the ZnS concentration increases from 25 to 200 mg/disc. The blank control disc produces no inhibition zone, confirming that bacterial growth inhibition is solely attributed to the antibacterial action of the ZnS ceramic material.

For Escherichia coli, the inhibition zone increases from 10.2 ± 0.4 mm at 25 mg/disc to 21.8 ± 0.6 mm at 200 mg/disc, indicating a continuous improvement in antibacterial efficiency with increasing ZnS concentration. A similar trend is observed for Staphylococcus aureus, where the inhibition diameter increases from 12.6 ± 0.5 mm to 24.6 ± 0.7 mm, representing the largest inhibition zone among all tested bacteria. This result demonstrates that *S. aureus* is the most susceptible bacterial strain toward ZnS ceramic materials.

For Pseudomonas aeruginosa, the inhibition zone gradually increases from 9.1 ± 0.3 mm to 17.9 ± 0.6 mm as the ZnS concentration increases. Although *P. aeruginosa* exhibits comparatively smaller inhibition zones than the other bacterial strains, substantial growth inhibition is still achieved at higher ZnS concentrations. Likewise, Bacillus subtilis exhibits inhibition diameters ranging from 11.4 ± 0.4 mm to 22.3 ± 0.6 mm, while Klebsiella pneumoniae shows inhibition zones increasing from 9.8 ± 0.4 mm to 18.9 ± 0.6 mm. These results confirm that ZnS ceramics possess broad-spectrum antibacterial activity against both Gram-positive and Gram-negative bacteria.

The lower section of Table 5 summarizes the quantitative bacterial survival determined using the Spread Plate Method (SPM). In contrast to the ADM results, where larger inhibition zones indicate stronger

*Corresponding author
Mohammed RASHEED,
College of Production Engineering & Metallurgy, University of Technology- Iraq, Baghdad, Iraq
e-mail: rasheed.mohammed40@yahoo.com

antibacterial activity, the SPM results demonstrate antibacterial efficiency through the progressive reduction in viable bacterial colonies. The untreated control exhibits the highest bacterial population for all investigated strains, with colony counts on the order of approximately 10^5 CFU $m.L^{-1}$. Following treatment with ZnS ceramics, the bacterial population decreases continuously with increasing ZnS concentration.

For Escherichia coli, the bacterial population decreases from 2.8×10^5 CFU $m.L^{-1}$ in the untreated control to 8.5×10^2 CFU $m.L^{-1}$ at the highest ZnS concentration. A similar reduction is observed for Staphylococcus aureus, where the colony count decreases from 2.6×10^5 to 5.6×10^2 CFU $m.L^{-1}$. Pseudomonas aeruginosa exhibits a reduction from 2.9×10^5 to 1.4×10^3 CFU $m.L^{-1}$, whereas Bacillus subtilis decreases from 2.4×10^5 to 4.2×10^2 CFU $m.L^{-1}$, and Klebsiella pneumoniae decreases from 2.7×10^5 to 7.6×10^2 CFU $m.L^{-1}$. The continuous reduction in bacterial colony counts confirms the strong bactericidal activity of ZnS ceramics.

The antibacterial efficiency obtained from the SPM measurements was calculated using Eq. 2

According to this equation, decreasing CFU values correspond to increasing antibacterial efficiency. Therefore, the lowest colony counts observed at 200 $\mu g.mL^{-1}$ indicate that ZnS ceramic materials achieve their highest antibacterial performance at the maximum investigated concentration.

A direct comparison between the ADM and SPM results presented in Table 5 reveals excellent agreement between the two antibacterial evaluation methods. Samples producing larger inhibition zones simultaneously exhibit lower bacterial colony counts, confirming that the qualitative observations obtained by the Agar Disc Method are fully supported by the quantitative bacterial survival measurements obtained using the Spread Plate Method. The consistency between these two independent techniques demonstrates the reliability and reproducibility of the antibacterial evaluation.

The concentration-dependent antibacterial activity observed in Table 5 is consistent with the antibacterial mechanism proposed in Fig. 12. Increasing ZnS concentration enhances the generation of reactive oxygen species (ROS) and the release of Zn^{2+} ions, resulting in greater membrane disruption, leakage of intracellular biomolecules, oxidative damage to proteins and DNA, and ultimately bacterial cell death. The experimental evidence supporting this mechanism, including ROS generation, membrane damage, intracellular leakage, and DNA fragmentation, was demonstrated previously in Fig. 13. Consequently, the quantitative results shown in Table 5 provide direct confirmation of the proposed antibacterial mechanism.

Furthermore, the excellent antibacterial performance correlates well with the structural characterization discussed throughout this study. The improved crystallinity observed by XRD (Fig. 4), the homogeneous particle morphology revealed by FESEM (Fig. 5), the stronger Zn–S bonding confirmed by FTIR (Fig. 9), and the enhanced lattice ordering demonstrated by Raman spectroscopy (Figs. 10 and 11) collectively contribute to more efficient ROS generation and stronger interaction between ZnS ceramic particles and bacterial cells. These structural improvements explain the enhanced antibacterial activity observed with increasing ZnS concentration. The quantitative antibacterial results presented in Table 5 demonstrate that ZnS ceramic materials possess excellent broad-spectrum antimicrobial activity against both Gram-positive and Gram-negative bacteria. The continuous increase in inhibition zone diameter together with the simultaneous reduction in bacterial colony counts confirms that the antibacterial performance is strongly concentration dependent. Among the investigated microorganisms, Staphylococcus aureus exhibits the highest susceptibility, whereas Pseudomonas aeruginosa shows comparatively greater resistance. Nevertheless, all bacterial strains are effectively inhibited at the highest ZnS concentration, highlighting the considerable potential of ZnS ceramic materials for antimicrobial coatings, biomedical implants, wound dressings, food-packaging materials, and water purification applications.

*Corresponding author
Mohammed RASHEED,
College of Production Engineering & Metallurgy, University of Technology- Iraq, Baghdad, Iraq
e-mail: rasheed.mohammed40@yahoo.com

Table 5. Quantitative antibacterial results of ZnS ceramic materials determined by the Agar Disc Method (ADM) as inhibition zone diameter (mm) and the Spread Plate Method (SPM) as bacterial colony count (CFU mL^{-1}) against five bacterial strains at different ZnS concentrations.

ADM: Zone of inhibition diameter (mm)

ZnS conc. (mg/disc)	Bacteria (ATCC strain)				
	E. coli 25922	*S. aureus* 25923	*P. aeruginosa* 27853	*B. subtilis* 6633	*K. pneumoniae* 700603
25	10.2 ± 0.4	12.6 ± 0.5	9.1 ± 0.3	11.4 ± 0.4	9.8 ± 0.4
50	13.7 ± 0.5	16.3 ± 0.5	11.8 ± 0.4	14.6 ± 0.5	12.3 ± 0.4
100	17.2 ± 0.6	20.1 ± 0.6	14.7 ± 0.5	18.5 ± 0.6	15.6 ± 0.5
200	21.8 ± 0.6	24.6 ± 0.7	17.9 ± 0.6	22.3 ± 0.6	18.9 ± 0.6
Control (Blank disc)	0	0	0	0	0

SPM: Colony count (CFU/mL)

ZnS conc. (µg/mL)	Bacteria (ATCC strain)				
	E. coli 25922	*S. aureus* 25923	*P. aeruginosa* 27853	*B. subtilis* 6633	*K. pneumoniae* 700603
0 (Control)	2.8×10^7	2.6×10^7	2.9×10^7	2.4×10^7	2.7×10^7
25	7.2×10^6	6.1×10^6	8.5×10^6	5.5×10^6	6.9×10^6
50	2.1×10^5	1.6×10^5	2.8×10^5	1.4×10^5	1.9×10^5
100	5.3×10^3	3.8×10^3	7.6×10^3	3.1×10^3	4.7×10^3
200	8.5×10^1	5.6×10^1	1.8×10^2	4.2×10^1	7.8×10^1

STATISTICAL ANALYSIS OF ANTIBACTERIAL ACTIVITY

The statistical analysis of the antibacterial activity of the ZnS ceramic materials determined using the Agar Disc Method (ADM) and the Spread Plate Method (SPM) is summarized in Table 6. The antibacterial results are expressed as mean ± standard deviation (SD) from three independent experiments (n = 3). Statistical comparisons among ZnS concentrations were performed using one-way analysis of variance (ANOVA) followed by Tukey's Honestly Significant Difference (HSD) post hoc test, while the relationship between the ADM and SPM results was evaluated using Pearson's correlation analysis. A significance level of $p < 0.05$ was considered statistically significant.

The statistical comparison of the ADM inhibition zone diameters presented in Table 6 demonstrates that ZnS concentration has a highly significant effect on the antibacterial activity against all investigated bacterial strains. The superscript letters (a–d) indicate statistically significant differences among the concentration groups, where values assigned different letters differ significantly ($p < 0.05$). Increasing the ZnS concentration from 25 to 200 mg/disc produces a continuous and statistically significant increase in the inhibition zone diameter for every bacterial strain. The largest inhibition zones are observed for Staphylococcus aureus, whereas Pseudomonas aeruginosa consistently exhibits the smallest inhibition zones, indicating comparatively greater bacterial resistance.

The SPM colony count data summarized in Table 6 exhibit an opposite but complementary trend. The untreated control possesses the highest bacterial population, while increasing ZnS concentration progressively reduces the number of viable bacterial colonies. Statistical analysis confirms that each increase in ZnS concentration significantly decreases bacterial survival ($p < 0.05$). At the highest ZnS concentration (200 µg.mL^{-1}), the colony counts are reduced by several orders of magnitude compared with the untreated control, confirming the strong bactericidal activity of ZnS ceramic materials.

The one-way ANOVA results presented in Table 6 demonstrate highly significant differences among the investigated concentration groups. For the ADM measurements, the calculated F-values range approximately from 291 to 413, whereas the corresponding p-values are less than 0.001 for every bacterial strain. Similar observations are obtained for the SPM measurements, where the calculated F-values are substantially higher (approximately 1533–2015) with $p < 0.001$. These results indicate that ZnS concentration exerts a statistically significant influence on both inhibition zone diameter and bacterial survival. Furthermore, the calculated effect size (η^2) ranges from approximately 0.991 to 0.999, indicating

*Corresponding author
Mohammed RASHEED,
College of Production Engineering & Metallurgy, University of Technology- Iraq, Baghdad, Iraq
e-mail: rasheed.mohammed40@yahoo.com

that more than 99% of the observed variation in antibacterial activity is explained by the ZnS concentration. Such exceptionally high effect sizes demonstrate the strong influence of ZnS dosage on antibacterial performance.

The Pearson correlation analysis summarized in Table 6 further demonstrates excellent agreement between the two antibacterial evaluation methods. The calculated correlation coefficients range from approximately −0.986 to −0.991, with $p < 0.001$ for all investigated bacterial strains. These results indicate an extremely strong negative correlation between the inhibition zone diameter determined by ADM and the bacterial colony count measured by SPM. Consequently, larger inhibition zones are consistently associated with lower bacterial survival, confirming the reliability and consistency of both antibacterial assessment techniques.

The antibacterial efficiency calculated from the SPM results is also summarized in Table 6. The antibacterial efficiency was determined according to Eq. 2

The calculated antibacterial efficiency increases progressively with ZnS concentration for all investigated bacterial strains. At the highest ZnS concentration (200 $\mu g.mL^{-1}$), the antibacterial efficiency exceeds 99.999% for most bacterial species, confirming the excellent bactericidal performance of the synthesized ZnS ceramic materials.

The statistical results summarized in Table 6 are fully consistent with the antibacterial mechanism proposed in Fig. 11 and the experimental evidence presented in Fig. 12. The statistically significant increase in inhibition zone diameter together with the corresponding reduction in bacterial colony count confirms that increasing ZnS concentration enhances reactive oxygen species (ROS) generation and Zn^{2+} ion release, thereby promoting membrane disruption, intracellular leakage, oxidative damage, and ultimately bacterial cell death. These biological processes explain the excellent antibacterial efficiencies observed for both Gram-positive and Gram-negative bacteria.

Furthermore, the outstanding antibacterial performance demonstrated statistically in Table 6 correlates well with the structural characteristics of the ZnS ceramics discussed in the previous sections. The improved crystallinity observed by XRD (Fig. 3), the homogeneous particle morphology revealed by FESEM (Fig. 4), the formation of strong Zn–S bonds confirmed by FTIR (Fig. 8), and the enhanced lattice ordering demonstrated by Raman spectroscopy (Figs. 9 and 10) collectively contribute to more efficient ROS generation and stronger interaction between ZnS particles and bacterial cells, thereby significantly improving the antibacterial The statistical analyses summarized in Table 6 confirm that ZnS ceramic materials exhibit highly significant concentration-dependent antibacterial activity against all investigated bacterial strains. The one-way ANOVA demonstrates highly significant differences among concentration groups ($p < 0.001$), while the exceptionally large effect sizes indicate that ZnS concentration is the dominant factor controlling antibacterial performance. Moreover, the very strong negative Pearson correlation ($r \approx -0.99$) between inhibition zone diameter and bacterial colony count confirms the excellent agreement between the ADM and SPM methods. These statistical findings provide robust quantitative evidence supporting the superior antibacterial performance of ZnS ceramic materials and reinforce their potential for advanced biomedical, environmental, and antimicrobial applications.

*Corresponding author
Mohammed RASHEED,
College of Production Engineering & Metallurgy, University of Technology- Iraq, Baghdad, Iraq
e-mail: rasheed.mohammed40@yahoo.com

Table 6. Statistical analysis of the antibacterial activity of ZnS ceramic materials obtained by the Agar Disc Method (ADM) and Spread Plate Method (SPM)

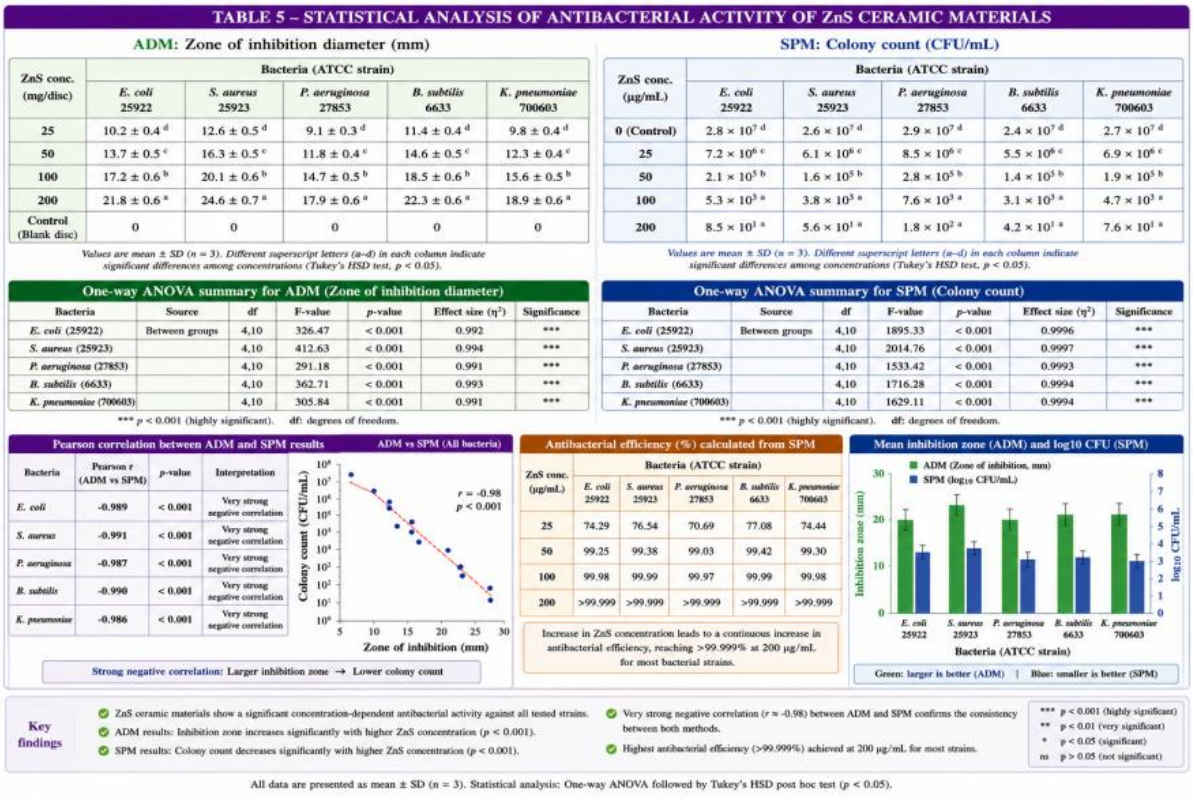

ANTIBACTERIAL EFFICIENCY (%) FROM ADM AND SPM DATA

The antibacterial efficiency of the synthesized ZnS ceramic materials was calculated from both the Agar Disc Method (ADM) and Spread Plate Method (SPM) results using the quantitative data summarized in Table 5. The calculated antibacterial efficiencies are graphically presented as three-dimensional plots in Fig. 15(a–b), while the corresponding statistical analyses are summarized in Table 6. These graphical representations provide a clearer visualization of the concentration-dependent antibacterial performance of ZnS ceramics against the investigated bacterial strains.

As illustrated in Fig. 15(a), the antibacterial efficiency determined from the ADM results increases continuously with ZnS concentration for all bacterial strains. The 3D representation clearly demonstrates that Staphylococcus aureus exhibits the highest antibacterial efficiency, whereas Pseudomonas aeruginosa shows comparatively lower susceptibility throughout the investigated concentration range.

The antibacterial efficiencies calculated from the SPM results are presented in Fig. 15(b). A continuous increase in antibacterial efficiency is observed as the ZnS concentration increases from 25 to 200 µg.m.L^{-1}, reaching values exceeding 99.999% for most bacterial strains at the highest concentration. The results shown in Fig. 15(b) are fully consistent with the reduction in bacterial colony counts summarized in Table 5.

A direct comparison between Fig. 15(a) and Fig. 15(b) indicates excellent agreement between the two antibacterial evaluation methods. Although the antibacterial efficiency is calculated from different experimental parameters (inhibition zone diameter for ADM and bacterial colony reduction for SPM), both methods demonstrate the same concentration-dependent antibacterial behavior and identify Staphylococcus aureus as the most susceptible bacterial strain. These observations are statistically supported by the results presented in Table 6, where highly significant differences ($p < 0.001$) and strong negative Pearson correlations ($r \approx -0.99$) confirm the consistency and reliability of both antibacterial evaluation techniques.

*Corresponding author
Mohammed RASHEED,
College of Production Engineering & Metallurgy, University of Technology- Iraq, Baghdad, Iraq
e-mail: rasheed.mohammed40@yahoo.com

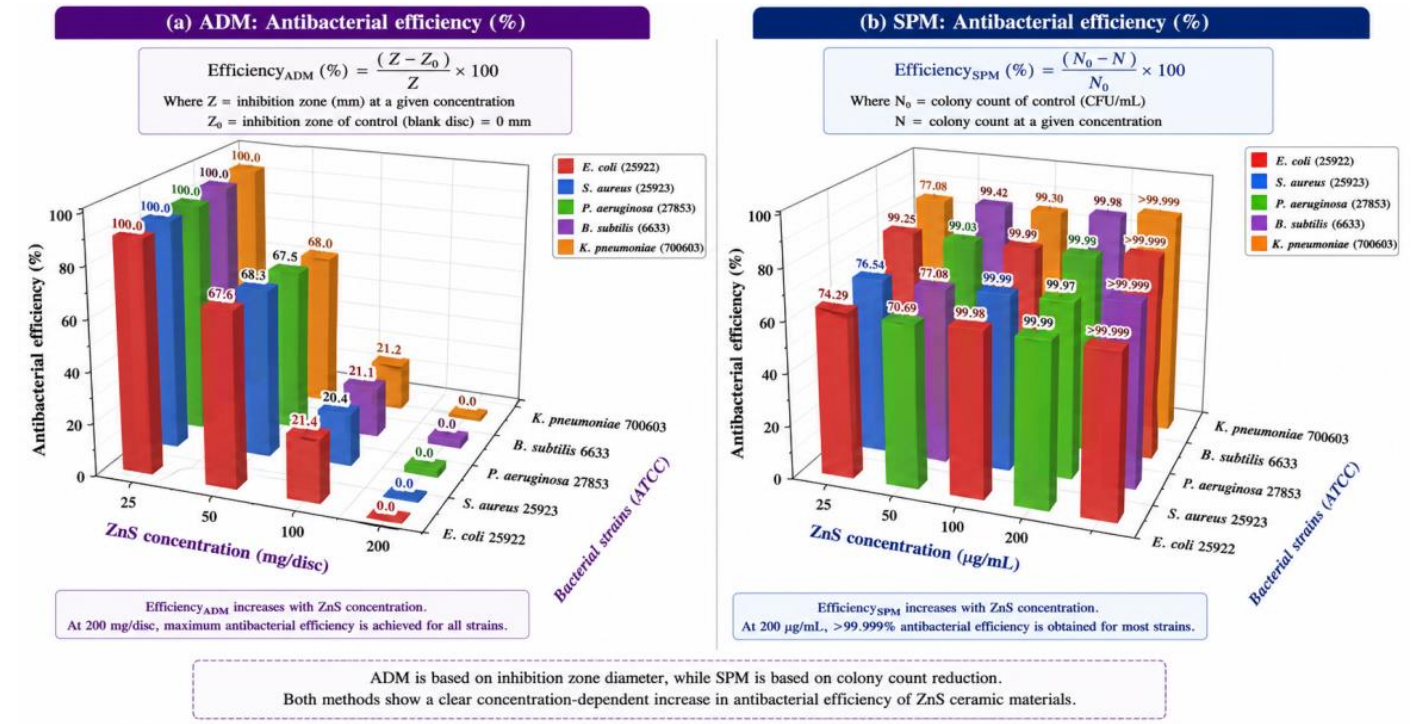

Fig. 15. Three-dimensional representation of the antibacterial performance of ZnS ceramic materials: (a) antibacterial activity based on the Agar Disc Method (ADM) and (b) antibacterial efficiency calculated from the Spread Plate Method (SPM) against five bacterial strains at different ZnS concentrations.

CONCLUSION

In this study, ZnS ceramic materials were successfully synthesized via the sol–gel method and thermally annealed at 500 °C and 700 °C to investigate the influence of heat treatment on their structural, morphological, optical, vibrational, and antibacterial properties. X-ray diffraction analysis confirmed the formation of a single-phase cubic zinc blende ZnS structure without detectable secondary phases, while thermal annealing significantly enhanced crystallinity, increased crystallite size, and reduced lattice microstrain and dislocation density. FESEM observations revealed uniformly distributed nanoparticles with improved particle growth and reduced agglomeration after annealing. EDX and elemental mapping verified the homogeneous distribution of Zn and S throughout the ceramic matrix, confirming the high compositional purity of the synthesized materials.

Optical characterization demonstrated excellent transparency in the visible region together with a direct optical band gap in the range of 3.72–3.80 eV, indicating that the optical properties can be effectively tailored through thermal treatment. FTIR and Raman analyses further confirmed the formation of strong Zn–S chemical bonds and improved lattice ordering, while the narrowing of Raman peaks and reduction in FWHM provided additional evidence of enhanced crystal quality after annealing.

The antibacterial investigation performed using both the Agar Disc Method (ADM) and the Spread Plate Method (SPM) demonstrated that ZnS ceramics possess excellent broad-spectrum antibacterial activity against Escherichia coli, Staphylococcus aureus, Pseudomonas aeruginosa, Bacillus subtilis, and Klebsiella pneumoniae. The antibacterial performance increased progressively with ZnS concentration, exhibiting larger inhibition zones, lower bacterial colony counts, and antibacterial efficiencies exceeding 99.999% at the highest concentration for most bacterial strains. Statistical analysis confirmed that these improvements were highly significant ($p < 0.001$) and strongly correlated with the enhanced structural properties of the ZnS ceramics.

The results demonstrate that thermal annealing is an effective strategy for improving the structural quality and antibacterial performance of ZnS ceramic materials. Owing to their excellent crystallinity, desirable optical characteristics, chemical stability, and outstanding antimicrobial activity, the synthesized ZnS

*Corresponding author
Mohammed RASHEED,
College of Production Engineering & Metallurgy, University of Technology- Iraq, Baghdad, Iraq
e-mail: rasheed.mohammed40@yahoo.com

ceramics represent promising candidates for advanced biomedical coatings, antimicrobial ceramics, healthcare devices, food-packaging systems, environmental disinfection, and water purification applications. Future studies should focus on evaluating cytocompatibility, long-term stability, biofilm inhibition, and photocatalytic antibacterial performance under visible-light irradiation to further expand the practical applications of ZnS ceramic materials.

REFERENCES

[1] K. P. V. Kumar, K. Shanmugam, and R. Ramamurthy, "Dye-sensitized solar cells with polyaniline: A review," Inorg. Chem. Commun., vol. 135, 109087, 2022. https://doi.org/10.1016/j.inoche.2021.109087.
[2] Z. Morshedtalab, G. Rahimi, A. Emami-Nejad, A. Farasat, A. Mohammadbeygi, N. Ghaedamini, and M. Negahdary, "Antibacterial assessment of zinc sulfide nanoparticles against Streptococcus pyogenes and Acinetobacter baumannii," Curr. Top. Med. Chem., vol. 20, no. 11, pp. 1042–1055, 2020. https://doi.org/10.2174/1381612826666200406095246.
[3] Y. Li, C. Liao, and S. C. Tjong, "Recent advances in zinc oxide nanostructures with antimicrobial activities," Int. J. Mol. Sci., vol. 21, no. 22, 8836, 2020. https://doi.org/10.3390/ijms21228836.
[4] M. S. Omar, M. N. M. N. M. Sanif, N. H. S. O. Ali, M. H. S. A. Hamid, H. Taha, A. H. Mahadi, Y. W. Soon, Z. Ngaini, M. Y. H. Rosli, and A. Usman, "Synthesis of Schiff base encapsulated ZnS nanoparticles: Characterization and antibacterial screening," Int. J. Technol., vol. 11, no. 7, pp. 1364–1375, 2020. https://doi.org/10.14716/ijtech.v11i7.4486.
[5] S. Kumar, S. Taneja, S. Banyal, M. Singhal, V. Kumar, S. Sahare, S. L. Lee, and R. K. Choubey, "Bio-synthesised silver nanoparticle-conjugated L-cysteine capped Mn:ZnS quantum dots for eco-friendly biosensor and antimicrobial applications," J. Electron. Mater., vol. 50, no. 7, pp. 3986–3995, 2021. https://doi.org/10.1007/s11664-021-08926-4.
[6] S. Göktaş, "Al-mediated doping boosts photocatalysis and room-temperature ferromagnetism in sol-gel ZnS thin films," J. Sol-Gel Sci. Technol., vol. 118, Art. no. 1, 2026. https://doi.org/10.1007/s10971-026-07150-y.
[7] M. F. Khan, M. H. Baig, A. Alotaibi, et al., "Anti-quorum sensing and anti-biofilm activity of zinc oxide nanospikes," ACS Omega, vol. 5, no. 50, pp. 32203–32215, 2020. https://doi.org/10.1021/acsomega.0c03634.
[8] A. Moghanian, M. Zohourfazeli, and M. H. M. Tajer, "The effect of zirconium content on in vitro bioactivity, biological behavior and antibacterial activity of sol-gel derived 58S bioactive glass," J. Non-Cryst. Solids, vol. 546, 120262, 2020. https://doi.org/10.1016/j.jnoncrysol.2020.120262.
[9] R. P. Sharma, S. D. Raut, A. S. Kadam, R. M. Mulani, and R. S. Mane, "In-vitro antibacterial and anti-biofilm efficiencies of chitosan-encapsulated zinc ferrite nanoparticles," Appl. Phys. A, vol. 126, 2020. https://doi.org/10.1007/s00339-020-04007-1.
[10] Y. Jeong, H. Kim, S. C. Lee, et al., "Facile eco-friendly sol-gel synthesis of highly monodispersed Zn@silica nanospheres with dual antibacterial mechanism against multidrug-resistant bacteria," Chem. Eng. J., vol. 531, 174108, 2026. https://doi.org/10.1016/j.cej.2026.174108.
[11] S. Pourmoslemi, F. Seif, and R. Mahjub, "Enhanced antibacterial activity of Ag-doped ZnS nanoparticles synthesised by a microwave-assisted polyol method," Mater. Res. Innov., vol. 25, no. 7, pp. 399–403, 2021. https://doi.org/10.1080/14328917.2020.1831151.
[12] Y. Zhou, T. Tong, X. Jiang, J. Liang, and S. Xiao, "GSH-ZnS nanoparticles exhibit high-efficiency and broad-spectrum antiviral activities via multistep inhibition mechanisms," ACS Appl. Bio Mater., vol. 3, no. 8, pp. 4809–4819, 2020. https://doi.org/10.1021/acsabm.0c00332.
[13] F. F. Al-Harbi, "Synthesis of Mn-doped ZnS nanoparticles and its characterization," J. Nanoelectron. Optoelectron., vol. 15, no. 1, pp. 65–70, 2020. https://doi.org/10.1166/jno.2020.2711.
[14] R. Rajendran and A. Mani, "Photocatalytic, antibacterial and anticancer activity of silver-doped zinc oxide nanoparticles," J. Saudi Chem. Soc., vol. 24, no. 12, pp. 1010–1024, 2020. https://doi.org/10.1016/j.jscs.2020.10.008.
[15] R. Perveen, S. Shujaat, Z. Qureshi, S. Nawaz, M. I. Khan, and M. Iqbal, "Green versus sol-gel synthesis of ZnO nanoparticles and antimicrobial activity evaluation against panel of pathogens," J. Mater. Res. Technol., vol. 9, no. 4, pp. 7817–7827, 2020. https://doi.org/10.1016/j.jmrt.2020.05.004.

*Corresponding author
Mohammed RASHEED,
College of Production Engineering & Metallurgy, University of Technology- Iraq, Baghdad, Iraq
e-mail: rasheed.mohammed40@yahoo.com

[16] M. Ijaz, M. Zafar, A. Islam, S. Afsheen, and T. Iqbal, "A review on antibacterial properties of biologically synthesized zinc oxide nanostructures," J. Inorg. Organomet. Polym. Mater., vol. 30, pp. 2815–2826, 2020. https://doi.org/10.1007/s10904-020-01603-9.
[17] A. F. Halbus, T. S. Horozov, and V. N. Paunov, "Surface-modified zinc oxide nanoparticles for antialgal and antiyeast applications," ACS Appl. Nano Mater., vol. 3, no. 1, pp. 440–451, 2020. https://doi.org/10.1021/acsanm.9b02045.
[18] R. P. Sharma, S. D. Raut, A. S. Kadam, R. M. Mulani, and R. S. Mane, "In-vitro antibacterial and anti-biofilm efficiencies of chitosan-encapsulated zinc ferrite nanoparticles," Appl. Phys. A, vol. 126, Art. no. 760, 2020. https://doi.org/10.1007/s00339-020-04007-1.
[19] M. S. Omar, M. N. M. N. M. Sanif, N. H. S. O. Ali, M. H. S. A. Hamid, H. Taha, A. H. Mahadi, Y. W. Soon, Z. Ngaini, M. Y. H. Rosli, and A. Usman, "Synthesis of Schiff base encapsulated ZnS nanoparticles: Characterization and antibacterial screening," Int. J. Technol., vol. 11, no. 7, pp. 1364–1375, 2020. https://doi.org/10.14716/ijtech.v11i7.4486.
[20] Z. Morshedtalab, G. Rahimi, A. Emami-Nejad, A. Farasat, A. Mohammadbeygi, N. Ghaedamini, and M. Negahdary, "Antibacterial assessment of zinc sulfide nanoparticles against Streptococcus pyogenes and Acinetobacter baumannii," Curr. Top. Med. Chem., vol. 20, no. 11, pp. 1042–1055, 2020. https://doi.org/10.2174/1381612826666200406095246.

[21] A. Zubaidi, Lamyaa Mahdi Asaad, Iqbal Alshalal, and M. Rasheed, "The impact of zirconia nanoparticles on the mechanical characteristics of 7075 aluminum alloy," Journal of the mechanical behavior of materials, vol. 32, no. 1, Jan. 2023, doi: https://doi.org/10.1515/jmbm-2022-0302.
[22] Djelel Kherifi, Ahcen Keziz, M. Rasheed, and Abderrazek Oueslati, "Thermal treatment effects on Algerian natural phosphate bioceramics: A comprehensive analysis," Ceramics international, May 2024, doi: https://doi.org/10.1016/j.ceramint.2024.05.317.
[23] A. Jaber, M. Ismael, T. Rashid, Mohammed Abdulhadi Sarhan, M. Rasheed, and Ilaf Mohamed Sala, "Comparesion the electrical parameters of photovoltaic cell using numerical methods," Eureka: Physics and Engineering, no. 4, pp. 29–39, Jul. 2023, doi: https://doi.org/10.21303/2461-4262.2023.002770.
[24] E. Kadri et al., "Ac conductivity and dielectric behavior of a−Si:H/c−Si1−yGey/p−Si thin films synthesized by molecular beam epitaxial method," Journal of Alloys and Compounds, vol. 705, pp. 708–713, May 2017, doi: https://doi.org/10.1016/j.jallcom.2017.02.117.
[25] M. Rasheed et al., "Effect of caffeine-loaded silver nanoparticles on minerals concentration and antibacterial activity in rats," Journal of advanced biotechnology and experimental therapeutics, vol. 6, no. 2, pp. 495–495, Jan. 2023, doi: https://doi.org/10.5455/jabet.2023.d144.
[26] M. Rasheed, O. Y. Mohammed, S. Shihab, and A. Al-Adili, "A comparative Analysis of PV Cell Mathematical Model," Journal of Physics: Conference Series, vol. 1795, no. 1, p. 012042, Mar. 2021, doi: https://doi.org/10.1088/1742-6596/1795/1/012042.
[27] M. Enneffati, B. Louati, K. Guidara, M. Rasheed, and R. Barillé, "Crystal structure characterization and AC electrical conduction behavior of sodium cadmium orthophosphate," Journal of Materials Science: Materials in Electronics, vol. 29, no. 1, pp. 171–179, Oct. 2017, doi: https://doi.org/10.1007/s10854-017-7901-7.
[28] Aasim Jasim Hussein, Mustafa Nuhad Al-Darraji, M. Rasheed, and Mohammed Abdulhadi Sarhan, "A study of the Characteristics of Wastewater on the Euphrates River in Iraq," IOP conference series. Earth and environmental science, vol. 1262, no. 2, pp. 022005–022005, Dec. 2023, doi: https://doi.org/10.1088/1755-1315/1262/2/022005.
[29] M. Enneffati, M. Rasheed, B. Louati, K. Guidara, and R. Barillé, "Morphology, UV–visible and ellipsometric studies of sodium lithium orthovanadate," Optical and Quantum Electronics, vol. 51, no. 9, Aug. 2019, doi: https://doi.org/10.1007/s11082-019-2015-5.
[30] A. A. Abdulrahman, M. Rasheed, and S. Shihab, "The Analytic of Image Processing Smoothing Spaces Using Wavelet," Journal of Physics: Conference Series, vol. 1879, no. 2, p. 022118, May 2021, doi: https://doi.org/10.1088/1742-6596/1879/2/022118.
[31] F. Dkhilalli, S. Megdiche, K. Guidara, M. Rasheed, R. Barillé, and M. Megdiche, "AC conductivity evolution in bulk and grain boundary response of sodium tungstate Na2WO4," Ionics, vol. 24, no. 1, pp. 169–180, Jul. 2017, doi: https://doi.org/10.1007/s11581-017-2193-8.

*Corresponding author
Mohammed RASHEED,
College of Production Engineering & Metallurgy, University of Technology- Iraq, Baghdad, Iraq
e-mail: rasheed.mohammed40@yahoo.com

[32] H. K. Aity, E. Dhahri, and M. Rasheed, "Optimization, dielectric properties, and antibacterial efficacy of copper-grafted MgO nanoparticles synthesized via sol-gel method," Ceramics International, 50 part B 54666-54687 Oct. 2024, doi: https://doi.org/10.1016/j.ceramint.2024.10.324.
[33] Tarek Saidani, M. Rasheed, Iqbal Alshalal, Arshad Abdula Rashed, Mohammed Abdelhadi Sarhan, and Regis Barille, "Characterization of thin ITO/Au/ITO sandwich films deposited on glass substrates using DC magnetron sputtering," Research on engineering structures & materials, Jan. 2023, doi: https://doi.org/10.17515/resm2023.21ma0922rs.
[34] M. Rasheed, S. Shihab, O. Alabdali, A. Rashid, and T. Rashid, "Finding Roots of Nonlinear Equation for Optoelectronic Device," Journal of Physics: Conference Series, vol. 1999, no. 1, p. 012077, Sep. 2021, doi: https://doi.org/10.1088/1742-6596/1999/1/012077.
[35] M. Rasheed and R. Barillé, "Comparison the optical properties for Bi2O3 and NiO ultrathin films deposited on different substrates by DC sputtering technique for transparent electronics," Journal of Alloys and Compounds, vol. 728, pp. 1186–1198, Dec. 2017, doi: https://doi.org/10.1016/j.jallcom.2017.09.084.
[36] W. Saidi, Nasreddine Hfaidh, M. Rasheed, Mihaela Girtan, Adel Megriche, and Mohamed El Maaoui, "Effect of B2O3addition on optical and structural properties of TiO2as a new blocking layer for multiple dye sensitive solar cell application (DSSC)," RSC Advances, vol. 6, no. 73, pp. 68819–68826, Jan. 2016, doi: https://doi.org/10.1039/c6ra15060h.
[37] T. Saidani, M. Zaabat, M. S. Aida, R. Barille, M. Rasheed, and Y. Almohamed, "Influence of precursor source on sol–gel deposited ZnO thin films properties," Journal of Materials Science: Materials in Electronics, vol. 28, no. 13, pp. 9252–9257, Mar. 2017, doi: https://doi.org/10.1007/s10854-017-6660-9.
[38] Aasim Jasim Hussein, Mustafa Nuhad Al-Darraji, and M. Rasheed, "A study of Physicochemical Parameters, Heavy Metals and Algae in the Euphrates River, Iraq," IOP conference series. Earth and environmental science, vol. 1262, no. 2, pp. 022007–022007, Dec. 2023, doi: https://doi.org/10.1088/1755-1315/1262/2/022007.
[39] A. Aukštuolis et al., "Measurement of charge carrier mobility in perovskite nanowire films by photo-celiv method," Proceedings of the Romanian Academy Series A - Mathematics Physics Technical Sciences Information Science, vol. 18, no. 1, pp. 34–41, 2017, Available: https://hal.archives-ouvertes.fr/hal-02443179.
[40] E. Kadri, M. Krichen, R. Mohammed, A. Zouari, and K. Khirouni, "Electrical transport mechanisms in amorphous silicon/crystalline silicon germanium heterojunction solar cell: impact of passivation layer in conversion efficiency," Optical and Quantum Electronics, vol. 48, no. 12, Nov. 2016, doi: https://doi.org/10.1007/s11082-016-0812-7.
[41] S. S. Batros, M. Rasheed, H. K. Aity, A. A. Hatef, and T. Saidani, "Tailoring the antibacterial efficiency of SnO2 nanoparticles through Cu doping," Materials Chemistry and Physics, vol. 355, p. 132243, May 2026, doi: https://doi.org/10.1016/j.matchemphys.2026.132243
[42] T. Saidani, S. Mokhtari, M. Rasheed, H. Lahmar, and M. Trari, "Annealing temperature dependent properties ZnO–TiO2 bilayer thin films: characteristics and photocatalytic activity," Journal of the Indian Chemical Society, vol. 103, no. 4, p. 102499, Apr. 2026, doi: https://doi.org/10.1016/j.jics.2026.102499.
[43] M. RASHEED and A. Khaleefah, "Sol–Gel-derived mullite nanoparticles: structural, antibacterial, and frequency-dependent impedance analysis," Materials Chemistry and Physics, p. 132112, Jan. 2026, doi: https://doi.org/10.1016/j.matchemphys.2026.132112.
[44] Z. S. Ahmed, M. RASHEED, and H. S. Ahmed, "Optimizing NiO nanoparticle properties for antibacterial applications via temperature-driven structural modification," Experimental and Theoretical NANOTECHNOLOGY, vol. 10, no. S, pp. 329–342, Feb. 2026, doi: https://doi.org/10.56053/10.s.329
[45] A. Raghdi, Menad Heraiz, M. Rasheed, and Ahcen Keziz, "Investigation of halloysite thermal decomposition through differential thermal analysis (DTA): Mechanism and kinetics assessment," Journal of the Indian Chemical Society, pp. 101413–101413, Oct. 2024, doi: https://doi.org/10.1016/j.jics.2024.101413.
[46] H. K. Aity, M. Rasheed, E. Dhahri, A. A. Hateef, and T. Saidani, "Chromium-doped magnesium oxide nanoparticles: dielectric insights and antibacterial potentials," Journal of Materials Science, vol. 61, no. 9, pp. 6226–6283, Jan. 2026, doi: https://doi.org/10.1007/s10853-026-12241-w.

*Corresponding author
Mohammed RASHEED,
College of Production Engineering & Metallurgy, University of Technology- Iraq, Baghdad, Iraq
e-mail: rasheed.mohammed40@yahoo.com

[47] Z. S. Ahmed, M. RASHEED, and H. S. Ahmed, "Enhancing α-Bi2O3 nanoparticle crystallinity and antibacterial functionality through controlled calcination," Experimental and Theoretical NANOTECHNOLOGY, vol. 10, no. S, pp. 343–356, Feb. 2026, doi: https://doi.org/10.56053/10.s.343.
[48] T. Rashid, M. M. Mokji, and M. Rasheed, "Cross-dataset evaluation of deep learning models for crack classification in structural surfaces," Journal of the Mechanical Behavior of Materials, vol. 34, no. 1, Jan. 2025, doi: https://doi.org/10.1515/jmbm-2025-0074.
[49] M. Rasheed, Iqbal Alshalal, Arshad Abdula Ashed, Mohammed Abdelhadi Sarhan, and Ahmed Shawki Jaber, "Mathematical models for resolving the nonlinear formula for solar cell," Indonesian journal of electrical engineering and computer science, vol. 33, no. 1, pp. 653–653, Jan. 2024, doi: https://doi.org/10.11591/ijeecs.v33.i1.pp653-660.
[50] F. BOUDOU et al., "Turmeric's protective effect on rats' prostate damage caused by aluminum," Notulae Scientia Biologicae, vol. 17, no. 3, p. 12593, Sep. 2025, doi: https://doi.org/10.55779/nsb17312593.
[51] M. Rasheed, M. N. Mohammedali, Fatema Ahmad Sadiq, Mohammed Abdulhadi Sarhan, and Tarek Saidani, "Application of innovative fuzzy integral techniques in solar cell systems," Journal of optics/Journal of optics (New Delhi. Print), Jun. 2024, doi: https://doi.org/10.1007/s12596-024-01928-5.
[52] Areej Adnan Hateef, Essebti Dhahri, M. Rasheed, Habiba Kadhim, Z. Abbas, and N. Hassan, "Study of the influence concentration difference of copper in properties of cerium nanopowder," Physics and Chemistry of Solid State, vol. 25, no. 4, pp. 801–810, Dec. 2024, doi: https://doi.org/10.15330/pcss.25.4.801-810.
[53] I. M. Mohammed and M. Rasheed, "An examination using semi-empirical methods to study how solvents influence the vibrational properties of the HCOOH molecule," AIP conference proceedings, vol. 3321, pp. 020026–020026, Jan. 2025, doi: https://doi.org/10.1063/5.0289719.
[54] R. S. Mahmood et al., "Leveraging normal distribution and fuzzy S-function approaches for solar cell electrical characteristic optimization," Journal of the Mechanical Behavior of Materials, vol. 34, no. 1, Jan. 2025, doi: https://doi.org/10.1515/jmbm-2025-0040.
[55] Farouk BOUDOU, Abdelmadjid GUENDOUZI, A. BELKREDAR, and M. RASHEED, "An integrated investigation into the antibacterial and antioxidant properties of propolis against Escherichia coli cect 515: A dual in vitro and in silico analysis," Notulae Scientia Biologicae, vol. 16, no. 2, pp. 13837–13837, May 2024, doi: https://doi.org/10.55779/nsb16211837.
[56] Ahcen Keziz, M. Rasheed, M. Heraiz, F. Sahnoune, and A. Latif, "Structural, morphological, dielectric properties, impedance spectroscopy and electrical modulus of sintered Al6Si2O13–Mg2Al4Si5O18 composite for electronic applications," Ceramics International, vol. 49, no. 23, pp. 37423–37434, Dec. 2023, doi: https://doi.org/10.1016/j.ceramint.2023.09.068.
[57] T. Rashid, Musa Mohd Mokji, and M. Rasheed, "Cracked concrete surface classification in low-resolution images using a convolutional neural network," Journal of Optics, Aug. 2024, doi: https://doi.org/10.1007/s12596-024-02080-w.
[58] A. Khaleefah and M. RASHEED, "Sol–gel-derived mullite nanoparticles: Structural and antibacterial insights," Experimental and Theoretical NANOTECHNOLOGY, vol. 10, no. S, pp. 289–300, Feb. 2026, doi: https://doi.org/10.56053/10.s.289
[59] Farouk BOUDOU, A. BELAKREDAR, Alaeddine BERKANE, and M. RASHEED, "Computational analysis and molecular dynamics of natural anthelmintic compounds from Algerian herbal sources," Notulae Scientia Biologicae, vol. 17, no. 2, pp. 12183–12183, Jun. 2025, doi: https://doi.org/10.55779/nsb17212183.
[60] E. Arif, R. Jamal, and M. RASHEED, "Performance enhancement of unsaturated polyester using sustainable CaCO3 nanoparticles: A multiscale characterization study," Experimental and Theoretical NANOTECHNOLOGY, vol. 10, no. 2, pp. 453–470, Apr. 2026, doi: https://doi.org/10.56053/10.2.453
[61] A. R. J. Katae, H. H. Hussein, A. S. Jaber, M. A. Sarhan, and M. RASHEED, "Fabrication and characterization of titanium dioxide thin films with various temperatures fabrication via sol-gel technique," Experimental and Theoretical NANOTECHNOLOGY, vol. 10, no. 2, pp. 795–809, Apr. 2026, doi: https://doi.org/10.56053/10.2.795
[62] Atheer. I. A. Ali and M. RASHEED, "Effect of changing magnetite percentage on structural and magnetic properties of cobalt ferrite prepared by the sol-gel method," Experimental and Theoretical NANOTECHNOLOGY, vol. 10, no. S, pp. 277–287, Feb. 2026, doi: https://doi.org/10.56053/10.s.277

*Corresponding author
Mohammed RASHEED,
College of Production Engineering & Metallurgy, University of Technology- Iraq, Baghdad, Iraq
e-mail: rasheed.mohammed40@yahoo.com

[63] Atheer. I. A. Ali and M. RASHEED, "Effect of sintering temperature on electrical and structural properties for spinel ferrites prepared by sol-gel method," Experimental and Theoretical NANOTECHNOLOGY, vol. 10, no. S, pp. 239–256, Feb. 2026, doi: https://doi.org/10.56053/10.s.239.

*Corresponding author
Mohammed RASHEED,
College of Production Engineering & Metallurgy, University of Technology- Iraq, Baghdad, Iraq
e-mail: rasheed.mohammed40@yahoo.com